

# Coherent Turbulence in the Boundary Layer of Hurricane Rita (2005) during an Eyewall Replacement Cycle

STEPHEN R. GUIMOND

*University of Maryland, Baltimore County, Baltimore, and NASA Goddard Space Flight Center, Greenbelt, Maryland*

JUN A. ZHANG

*University of Miami, Coral Gables, and NOAA/Hurricane Research Division, Miami, Florida*

JOSEPH W. SAPP

*Global Science and Technology, Inc., and NOAA/NESDIS/STAR, College Park, Maryland*

STEPHEN J. FRASIER

*Microwave Remote Sensing Laboratory, University of Massachusetts Amherst, Amherst, Massachusetts*

(Manuscript received 20 November 2017, in final form 22 May 2018)

## ABSTRACT

The structure of coherent turbulence in an eyewall replacement cycle in Hurricane Rita (2005) is presented from novel airborne Doppler radar observations using the Imaging Wind and Rain Airborne Profiler (IWRAP). The IWRAP measurements and three-dimensional (3D) wind vector calculations at a grid spacing of 250 m in the horizontal and 30 m in the vertical reveal the ubiquitous presence of organized turbulent eddies in the lower levels of the storm. The data presented here, and the larger collection of IWRAP measurements, currently are the highest-resolution Doppler radar 3D wind vectors ever obtained in a hurricane over the open ocean. Coincident data from NOAA airborne radars, the Stepped Frequency Microwave Radiometer, and flight-level data help to place the IWRAP observations into context and provide independent validation. The typical characteristics of the turbulent eddies are the following: radial wavelengths of  $\sim 1\text{--}3$  km (mean value is  $\sim 2$  km), depths from the ocean surface up to flight level ( $\sim 1.5$  km), aspect ratio of  $\sim 1.3$ , and horizontal wind speed perturbations of  $10\text{--}20$  m s $^{-1}$ . The most intense eddy activity is located on the inner edge of the outer eyewall during the concentric eyewall stage with a shift to the inner eyewall during the merging stage. The evolving structure of the vertical wind shear is connected to this shift and together these characteristics have several similarities to boundary layer roll vortices. However, eddy momentum flux analysis reveals that high-momentum air is being transported upward, in contrast with roll vortices, with large positive values ( $\sim 150$  m $^2$  s $^{-2}$ ) found in the turbulent filaments. In the decaying inner eyewall, elevated tangential momentum is also being transported radially outward to the intensifying outer eyewall. These results indicate that the eddies may have connections to potential vorticity waves with possible modifications due to boundary layer shear instabilities.

## 1. Introduction

Significant strides have been made in our understanding of the tropical cyclone (TC), but several issues still impede our ability to advance the science, including

- 1) lack of substantial (dense volumes of data in space/time), high-resolution observations on the scales of convection and turbulence;

- 2) incomplete knowledge of the physics on a multitude of scales, which can lead to improper representation of physical processes in numerical models; and
- 3) difficulty in solving a system of coupled, nonlinear, partial differential equations (e.g., numerical approximations in space/time and the issue of predictability).

Specific areas of TC science with gaps in understanding, and the associated largest problems with forecasting, include genesis, rapid intensification, and the evolution of eyewall replacement cycles (e.g., Gall et al. 2013). The lower levels of the storm, including the boundary layer,

---

*Corresponding author:* Stephen R. Guimond, sguimond@umbc.edu

play a central role in operational forecasting and critically govern the dynamics at all stages of the system life cycle (e.g., Emanuel 1995; Black et al. 2007; Bryan and Rotunno 2009; Smith and Montgomery 2010; Kepert 2012; Zhu et al. 2014; Zhang et al. 2015). For example, turbulent eddies are associated with TC intensity and structure change through the redistribution of thermal energy, momentum, and moisture in the TC boundary layer in both the horizontal and vertical directions (e.g., Bryan 2012; Rotunno and Bryan 2012). This turbulent transport affects both the system-scale energetics as well as convective-scale processes that rely on fluxes of heat and moisture from the ocean surface (e.g., Emanuel 1986). One manifestation of turbulent eddies in the TC boundary layer are roll vortices (Foster 2005), which have been studied through in situ observations (Zhang et al. 2008, 2011a), ground-based radar measurements (Wurman and Winslow 1998; Morrison et al. 2005; Lorsolo et al. 2008), synthetic aperture radar measurements (Zhang et al. 2008; Li et al. 2013), and numerical simulations (Zhu 2008; Nakanishi and Niino 2012; Gao and Ginis 2016; Gao et al. 2017). Recent theories for TC intensification have focused on the boundary layer as a fundamental mechanism in the spinup of the TC through the contributions of unbalanced flow and the connection to the bulk vortex aloft through updrafts (e.g., Smith and Montgomery 2010).

Measurements of the hurricane boundary layer are difficult to obtain and have relied heavily on in situ wind profiles obtained via global positioning system dropsondes. Over time, these data have documented the structure of the mean wind profile as a function of storm radial distance (e.g., Franklin et al. 2003). In addition, compositing of dropsonde data has provided an understanding of the azimuthal-mean TC structure in the boundary layer (e.g., Bell and Montgomery 2008). While a valuable source of wind information, the Lagrangian nature of the dropsonde (not a true vertical profile) and coarse horizontal sampling provides limitations for analyzing the structure and dynamics of TCs. Calculations of the three wind components over dense, high-resolution volumes of the atmosphere from airborne Doppler radars represent more of a true vertical profile, which is useful for hurricane dynamics research that involves the calculation of derivatives. However, airborne radars are not without difficulties, as surface scattering and coarse sampling often obscures the boundary layer, and measurements are only available where precipitation particles can be tracked. Airborne radars are highly complicated systems, but the payoff for atmospheric research can be significant.

In this paper, we present a unique set of airborne Doppler radar observations of the lower levels (down to  $\sim 200$ -m height) of Hurricane Rita (2005) during an

eyewall replacement cycle with an unprecedented resolution (grid spacing of 250 m in the horizontal and 30 m in the vertical). These new observations are placed into context with additional measurements from the NOAA WP-3D aircraft including tail Doppler radar, lower-fuselage radar, Stepped Frequency Microwave Radiometer (SFMR), and in situ data. The goal of the observations and analyses presented here is to address TC science challenges 1 and 2 described above. Details of the measurements and calculations are described in section 2. An overview of Hurricane Rita (2005) during the storm's concentric eyewall cycle including an explanation of prior work is described in section 3. Results from the new Imaging Wind and Rain Airborne Profiler (IWRAP) radar analyses and their connection to the eyewall replacement cycle in Rita is presented in section 4. Section 5 analyzes the nature of the turbulent scales of motion captured by IWRAP in relation to prior theoretical work. Finally, section 6 summarizes the important findings, and implications for TC science are discussed.

## 2. Data and processing

### a. IWRAP

For several years, the University of Massachusetts Amherst has deployed a Doppler radar on the NOAA WP-3D (P-3) research aircraft called the IWRAP (Fernandez et al. 2005). The IWRAP is a downward-pointing, conically scanning, dual-frequency, dual-polarization Doppler radar that measures surface backscatter and intervening volume reflectivity and Doppler velocity at 30-m range resolution. The radar operates simultaneously at two programmable incidence angles, and can alternate between horizontal and vertical polarizations. Figure 1 illustrates the measurement technique employed by this instrument as well as the SFMR collocated with IWRAP on the NOAA P-3 aircraft.

Using frequency-scanned phased-array antennas at both C- and Ku-band, the incidence angle may be adjusted from  $25^\circ$  to  $50^\circ$  incidence with a typical azimuthal scan rate of 60 revolutions per minute (rpm). The Ku-band antenna is a scaled version of the C-band antenna, therefore providing very similar beam characteristics. The Ku- and C-band antennas (single-polarized for this study) have 3-dB azimuthal (elevation) beamwidths of  $8.3^\circ$  ( $5.1^\circ$ ) and  $4.5^\circ$  ( $4.8^\circ$ ), respectively, at  $30^\circ$  incidence. The Ku-band footprint at the surface for the  $30^\circ$  incidence angle is on average  $\sim 200$  m.

In this study, we focus on Ku-band Doppler velocities because of the ability to compute winds at a lower altitude than the C-band antenna. The C-band antenna has a more prominent sidelobe structure than Ku-band, which creates a deeper surface scattering signature.

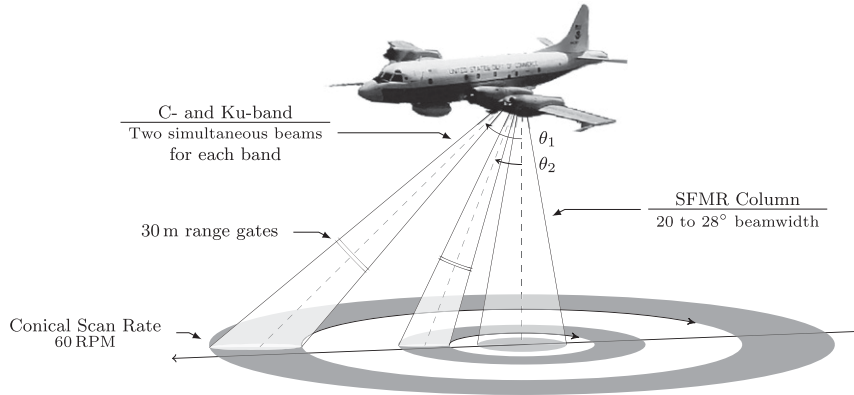


FIG. 1. Measurement geometry of the conically scanning IWRAP and nadir-viewing SFMR instruments on the NOAA WP-3D aircraft.

In addition, we focus on the inner-beam ( $30^\circ$  incidence) data, which, when combined with the Ku-band Doppler velocities, allow wind retrievals down to  $\sim 200$ -m height with a swath width at the surface of  $\sim 1.75$ – $2.30$  km. The NOAA P-3 aircraft had a typical flight altitude of  $1.5$ – $2$  km and an airspeed of  $\sim 100$ – $150$   $\text{m s}^{-1}$  for the data presented here. The Ku-band signal will experience attenuation in the lower levels of intense hurricanes, but quality Doppler velocities are still attainable in most cases, albeit at a higher uncertainty. The C-band data can be used to augment the Ku-band data in regions of severe attenuation. More details on the IWRAP system specifications can be found in [Fernandez et al. \(2005\)](#).

IWRAP is calibrated via both internal and external methods. During radar operation, an internal calibration loop injects an attenuated version of the transmitted signal directly into the receiver thus enabling monitoring of any drifts in transmitter power or in receiver gain. External calibration is achieved by combining ground calibration measurements with a final adjustment computed from a scatterometer geophysical model function using collocated SFMR measurements. For a description of the external calibration method, see [Sapp et al. \(2013, 2016\)](#).

The main advantage of IWRAP for understanding the lower levels of TCs, including the boundary layer, is the

*unprecedented wind and radar reflectivity resolution.* Retrievals of the three Cartesian wind components (hereafter 3D winds) across the entire IWRAP sampling volume can be computed using the variational algorithm outlined in [Guimond et al. \(2014\)](#). The typical along-track sampling of IWRAP is  $\sim 100$ – $150$  m, which allows wind calculations and mapped radar reflectivity with a horizontal grid spacing of  $\sim 150$ – $250$  m and 30-m vertical spacing. In this paper, we use a horizontal grid spacing of 250 m. These grid intervals currently provide the highest-resolution 3D radar wind retrievals ever obtained in a hurricane over the open ocean.

[Guimond et al. \(2014\)](#) mapped the radar spherical coordinates to Earth-relative coordinates to compute the winds on a storm-relative grid. Through the IWRAP validation efforts described in this paper, an error in the Earth-relative equations of [Guimond et al. \(2014\)](#) was found, which stems from an error in the methodology of [Lee et al. \(1994\)](#). The Earth-relative equations of [Lee et al. \(1994\)](#) [see their (15)] have no dependence on the aircraft drift angle, which will produce wind directions that are in error by the drift angle. This error does not affect the wind magnitude. The simple fix is to replace the heading angle with the track angle in (15) of [Lee et al. \(1994\)](#) and (5) of [Guimond et al. \(2014\)](#). The new Earth-relative equations for the IWRAP geometry at range  $r$  are given by

$$\begin{pmatrix} x \\ y \\ z \end{pmatrix} = r \begin{bmatrix} \cos T(a) + \sin T \sin \tau(b) + \sin T(c) \\ -\sin T(a) + \cos T \sin \tau(b) + \cos T(c) \\ \sin \tau(\sin P \cos \theta - \cos P \sin R \sin \theta) - \cos P \cos R \cos \tau \end{bmatrix}, \quad (1)$$

where

$$\begin{pmatrix} a \\ b \\ c \end{pmatrix} = \begin{pmatrix} \cos R \sin \theta \sin \tau - \sin R \cos \tau \\ \cos P \cos \theta + \sin P \sin R \sin \theta \\ \sin P \cos R \cos \tau \end{pmatrix} \quad (2)$$

and  $T$ ,  $P$ ,  $R$ ,  $\theta$ , and  $\tau$  are the track, pitch, roll, azimuth, and tilt angles, respectively.

In this paper, the winds are computed on an aircraft track–relative grid to enable higher-quality data display and to minimize interpolation errors. The track-relative

coordinates ( $x_t$ ,  $y_t$ ; cross track and along track, respectively) for the IWRAP geometry are given by

$$\begin{pmatrix} x_t \\ y_t \end{pmatrix} = r \begin{bmatrix} \cos D(a) - \sin D \sin \tau(b) - \sin D(c) \\ \sin D(a) + \cos D \sin \tau(b) + \cos D(c) \end{bmatrix}, \quad (3)$$

where  $D$  is the drift angle and the vertical coordinate  $z$  is defined in (1). Equation (3) is derived for the IWRAP geometry following Lee et al. (1994), and all angle conventions and coordinate systems follow this paper as well. The inversion for the 3D winds still requires the Earth-relative coordinates [(1) and (2)] to compute the observation error term  $\mathbf{J}_o$  in the cost function

$$\mathbf{J} = \mathbf{J}_o + \alpha_M \left\| \frac{\partial u}{\partial x} + \frac{\partial v}{\partial y} + \frac{1}{\rho} \frac{\partial \rho w}{\partial z} \right\|^2 + \alpha_s \|\nabla^2 \cdot \mathbf{u}\|^2, \quad (4)$$

where  $u$ ,  $v$ , and  $w$  are the Cartesian velocities,  $\rho = \rho(z)$  is an environmental density profile, and  $\mathbf{u}$  is the three-dimensional wind vector. The double vertical bars represent the Euclidean norm. In this paper, a value of  $2\Delta x^2$  for  $\alpha_M$  (anelastic mass continuity weight) and 0 for  $\alpha_s$  (Laplacian spatial filter) were chosen, where  $\Delta x$  is the horizontal grid spacing of the analysis. Solutions for the wind field are found by evaluating the function and gradient of (4) with respect to the parameters,  $\partial \mathbf{J} / \partial \mathbf{u}$ , and feeding this information into a nonlinear minimization code (Guimond et al. 2014). A two-point (500 m) along-track running mean was applied to the 3D winds after the solution process to filter grid-scale noise. Hydrometeor fall speeds are computed and removed from the Doppler velocities before the solution for the wind field using the rain relations of Ulbrich and Chilson (1994) projected onto the IWRAP beams,  $V_r^c = V_r^u - f \cos(\tau)$ , where  $V_r^u$  and  $V_r^c$  are the uncorrected and corrected Doppler velocities, respectively, and  $f$  are the rain fall speeds. Other details of the wind retrieval algorithm, including the exact form of  $\mathbf{J}_o$ , can be found in Guimond et al. (2014).

Validation of the algorithm with simulated and limited in situ data was presented in Guimond et al. (2014). Here, an extensive validation of the IWRAP wind retrievals in Hurricane Rita (2005) was performed using in situ flight-level data. To make the comparisons, the 1-Hz flight-level data is interpolated to a 250-m along-track grid to match the IWRAP wind retrievals. Note that the IWRAP sampling volume is approximately equal to the flight-level sampling interval. The typical height of the flight-level data was  $\sim 1.5$  km, while the first level of useful IWRAP data was  $\sim 1.4$  km. All IWRAP data at  $\sim 1.4$ -km height on 22 September and two passes on 23 September were used in the validation. Low signal-to-noise ratio (SNR) data were not included.

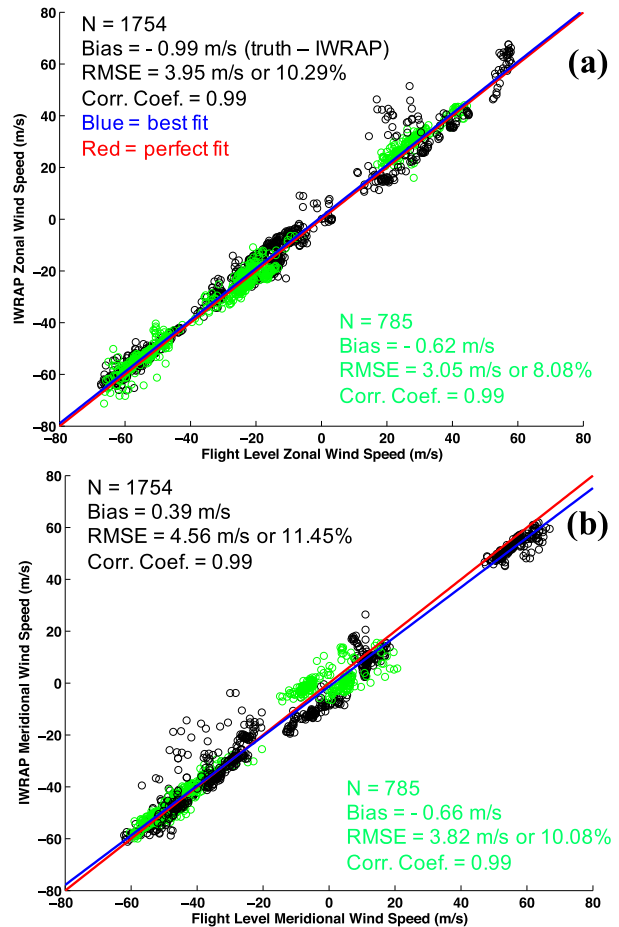


FIG. 2. Comparison of flight-level horizontal wind vectors to IWRAP-computed horizontal wind vectors for (a) zonal wind speed and (b) meridional wind speed. The black points include the majority of the Rita data with green points denoting data for the flight legs displayed in the paper. See text for more details.

Figures 2a and 2b show scatterplots and best-fit lines for comparisons of the zonal and meridional wind speed, respectively. The validation statistics show good agreement between IWRAP horizontal wind vectors and the flight-level data. For all the data, the zonal (meridional) wind speeds were found to have root-mean-square errors (RMSEs) of  $3.95 \text{ m s}^{-1}$  ( $4.56 \text{ m s}^{-1}$ ), which is  $\sim 10\%$ – $12\%$  of the sampled wind speed. For the specific flight legs presented in this paper, the errors are lower ( $\sim 8\%$ – $10\%$ ). It is clear from Fig. 2 that the IWRAP-computed horizontal wind vectors are able to resolve the turbulent perturbations in the flight-level data very well with correlation coefficients of 0.99.

The vertical wind speed is a more difficult component to measure/calculate because of several issues: the small values relative to the horizontal wind, which makes them susceptible to small errors in other parts of the system such as the antenna-pointing direction, and

the strong dependence on uncertain hydrometeor fall speeds. As a result, the vertical wind speed was evaluated on a leg-by-leg basis with the validation results for the flight legs described in this paper presented in Fig. 3. The IWRAP data for the 2030–2040 UTC 22 September 2005 flight leg (Fig. 8) were found to have a significant high bias ( $\sim 2.8 \text{ m s}^{-1}$ ), which was a rare occurrence, and that correction was applied in Fig. 3. Figure 3 shows that overall, the IWRAP data have a slight high bias ( $0.75 \text{ m s}^{-1}$ ) relative to the flight-level data with an RMSE of  $1.94 \text{ m s}^{-1}$  or 124% and a correlation coefficient of 0.65. These error statistics are similar to those from the NOAA P-3 tail Doppler radar (Reasor et al. 2009).

### b. SFMR

The NOAA Aircraft Operations Center (AOC) SFMR provides estimates of the 10-m neutral stability wind speed and the column-integrated rain rate (Uhlhorn and Black 2003; Uhlhorn et al. 2007; Klotz and Uhlhorn 2014). The SFMR operates by measuring the radiometric brightness temperature at nadir over a range of frequencies within C band ( $\sim 4\text{--}7 \text{ GHz}$ ). The nadir brightness temperature is dependent upon both the emission from the surface and the intervening attenuation and emission by precipitation within the atmospheric column. The wind speed sensitivity of the SFMR is governed primarily by the presence of foam on the sea surface. Experience has shown that the accuracy of wind estimates improves as surface winds exceed approximately  $15\text{--}20 \text{ m s}^{-1}$  (e.g., Uhlhorn and Black 2003). At lower wind speeds the fractional foam coverage is small. The SFMR makes a new brightness temperature measurement at up to two out of the six channels and corresponding wind speed retrieval at a 1-Hz rate. However, the 1-Hz wind speeds are not independent of the previous measurement, which is equivalent to a  $\sim 100\text{--}150\text{-m}$  along-track running mean based on typical P-3 airspeeds. The 3-dB main beamwidth of the SFMR varies between  $\sim 20^\circ$  and  $\sim 28^\circ$  (see Fig. 1), which results in a footprint at the ocean surface of  $\sim 550\text{--}750 \text{ m}$  for a typical P-3 altitude during the flights described in this paper ( $\sim 1.5 \text{ km}$ ).

### c. NOAA tail and lower-fuselage radars

The NOAA P-3 tail (TA) airborne Doppler radar operates at X-band and scans in a cone  $20^\circ$  fore and aft of the plane perpendicular to the aircraft with a scan rate of 10 rpm and along-track sampling of  $\sim 1.6 \text{ km}$  (Gamache et al. 1995). Three-dimensional wind vector calculations are performed using the variational methodology outlined in Gamache (1997) and Reasor et al. (2009) at a grid spacing of 2 km in the horizontal and 0.5 km in the vertical.

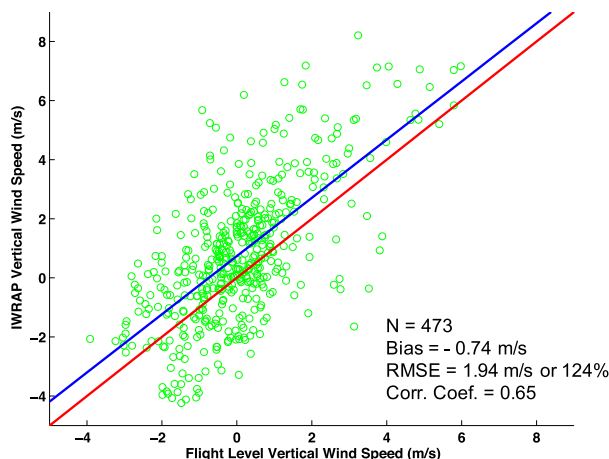


FIG. 3. As in Fig. 2, but showing vertical wind speed comparisons for the flight legs displayed in the paper. Note that radar data with low signals are discarded for these comparisons. See text for more details.

A C-band lower-fuselage (LF) radar that provides a fast scan of radar reflectivity every 30 s over a large horizontal domain at the flight-level height is also carried aboard the P-3 aircraft. The LF radar dataset is useful for identifying vortex- and convective-scale features of TCs and examining their time evolution close to the aircraft. In this paper, analysis of LF data is limited to ranges less than 50 km to avoid problems associated with the large vertical beamwidth ( $4.1^\circ$ ) of the C-band antenna, such as inadequate beam filling and smearing of features for ranges greater than  $\sim 60 \text{ km}$ . Storm center estimates for all the data presented in this paper are provided by NOAA's Hurricane Research Division (HRD), utilizing the methodology of Willoughby and Chelmow (1982).

## 3. Overview of Hurricane Rita (2005) during observation period

The IWRAP radar sampled Hurricane Rita for the 5-h period between 1700 and 2200 UTC on both 22 and 23 September 2005 when the storm was undergoing an eyewall replacement cycle. The peak intensity of Rita reached category 5 status with maximum sustained winds of  $\sim 80 \text{ m s}^{-1}$  and a minimum central pressure of 897 hPa at  $\sim 0600 \text{ UTC}$  22 September (Knabb et al. 2006). The storm environment was very conducive for producing intense TCs with high sea surface temperatures ( $\sim 30^\circ\text{C}$ ) and low vertical wind shear ( $\sim 5 \text{ m s}^{-1}$ ) as noted by Bell et al. (2012). However, the inner-core dynamics of the storm dominated the system evolution during the IWRAP sampling interval as Rita began to weaken because of an eyewall replacement cycle.



Nevertheless, Rita remained a powerful hurricane during the observation period with maximum sustained winds estimated by the National Hurricane Center (NHC) of  $\sim 60\text{--}65\text{ m s}^{-1}$  on 22 September and  $\sim 55\text{ m s}^{-1}$  on 23 September. Further details on the storm life cycle can be found in Knabb et al. (2006), Didlake and Houze (2011), and Bell et al. (2012).

Bell et al. (2012) examined the axisymmetric evolution of Rita for a  $\sim 24\text{-h}$  period starting at 1800 UTC 21 September from a unique set of observations with a focus on the ELDORA airborne radar during a concentric eyewall stage of the storm. During this time period, the authors found that the outer eyewall intensified and contracted while the inner eyewall decayed. Despite the decay of the inner core, it remained very intense and dominated the mean vortex structure. The authors proposed that a large rainband with elevated cyclonic vorticity near 80-km radius played a significant role in the formation of the secondary eyewall. In addition, the observations and analyses indicated that both balanced and unbalanced processes played a role in the tangential wind evolution in both eyewalls.

Didlake and Houze (2011) examined the axisymmetric and asymmetric secondary eyewall of Hurricane Rita (2005) between 1800 and 1820 UTC 22 September using ELDORA airborne radar data. They showed alternating signed bands of vorticity in the primary and secondary eyewall of Rita during this time period and suggested that vortex Rossby waves may be active in the storm. These banded vorticity features had wavelengths of 6–10 km and were nearly collocated with like-signed vertical velocity perturbations, indicating coupling to the convective field.

#### 4. Radar measurements and analysis

##### a. 1700–2200 UTC 22 September

Figure 4 shows an LF radar reflectivity scan of Rita ( $\sim 1.5\text{-km}$  height) during the middle of this sampling period at 1936 UTC 22 September when the storm was slowly weakening because of an eyewall replacement cycle. A well-defined axisymmetric outer eyewall is apparent at a radius of  $\sim 40\text{--}50\text{ km}$  along with an asymmetric inner eyewall at a radius of  $\sim 15\text{--}20\text{ km}$ . The most intense reflectivity is located in the northern and northwestern portions of the inner eyewall. Radial oscillations in reflectivity are also noted in the northern portions of the storm between the inner and outer eyewalls with a wavelength of  $\sim 8\text{--}10\text{ km}$ . These banded structures were observed to propagate both radially and azimuthally in LF radar reflectivity animations (not shown) during the observation period. As discussed in

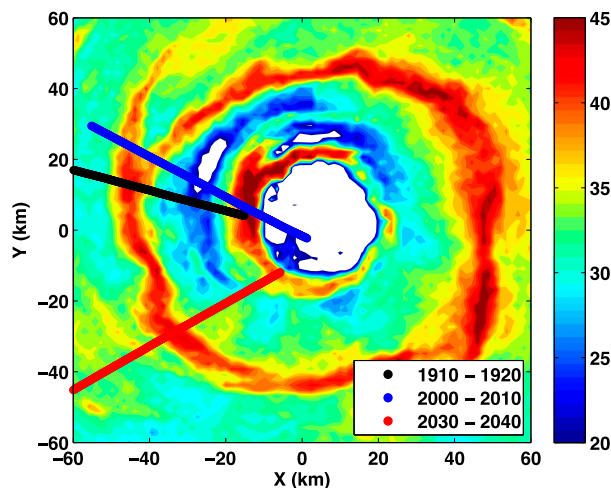


FIG. 4. Horizontal cross section ( $\sim 1.5\text{-km}$  height) of radar reflectivity (C band) in Hurricane Rita at  $\sim 1936$  UTC 22 Sep 2005 from the lower-fuselage radar on the NOAA P-3 aircraft. The colored lines denote the flight tracks of the P-3 aircraft on 22 Sep 2005 where IWRAP data are analyzed.

section 3, Didlake and Houze (2011) showed vorticity anomalies (see their Fig. 3d) with similar wavelengths as the reflectivity features observed here in Fig. 4.

Figure 5 shows total horizontal wind speed and vertical velocity from the P-3 TA radar at 1-km height for the three time periods corresponding to the radial legs shown in Fig. 4. The vertical level and fields shown in Fig. 5 were chosen to highlight the larger-scale structure of the storm at low levels as a prelude to the presentation of the IWRAP observations. Note that TA radar data at 0.5-km height were also analyzed, but the coverage was more limited at this level and the fields looked very similar to those at 1-km height.

A distinct double wind maximum is evident in the P-3 TA wind speeds corresponding to the concentric eyewall reflectivity structure shown in Fig. 4. The maximum wind speeds in the TA domain from 1.5 km to the lowest analysis level of 0.5 km are  $\sim 68\text{ m s}^{-1}$  at 1927 UTC,  $\sim 71\text{ m s}^{-1}$  at 2015 UTC, and  $\sim 57\text{ m s}^{-1}$  at 2030 UTC. The inner eyewall has weaker vertical motion ( $\sim 0.5\text{--}1\text{ m s}^{-1}$ ) at all times compared to the outer eyewall ( $2\text{--}3\text{ m s}^{-1}$ ) with noteworthy regions of descent approaching  $-2\text{ m s}^{-1}$  evident at 2015 and 2030 UTC. This is consistent with an intensifying outer eyewall and decaying inner eyewall even though the inner eyewall is still the most intense feature (Didlake and Houze 2011; Bell et al. 2012).

The P-3 aircraft completed  $\sim 15$  radial legs through the storm center during the 1700–2200 UTC time period with high-quality IWRAP data gathered in the majority of those legs found mostly in the northwestern portion of the storm. Three of those radial legs are analyzed here

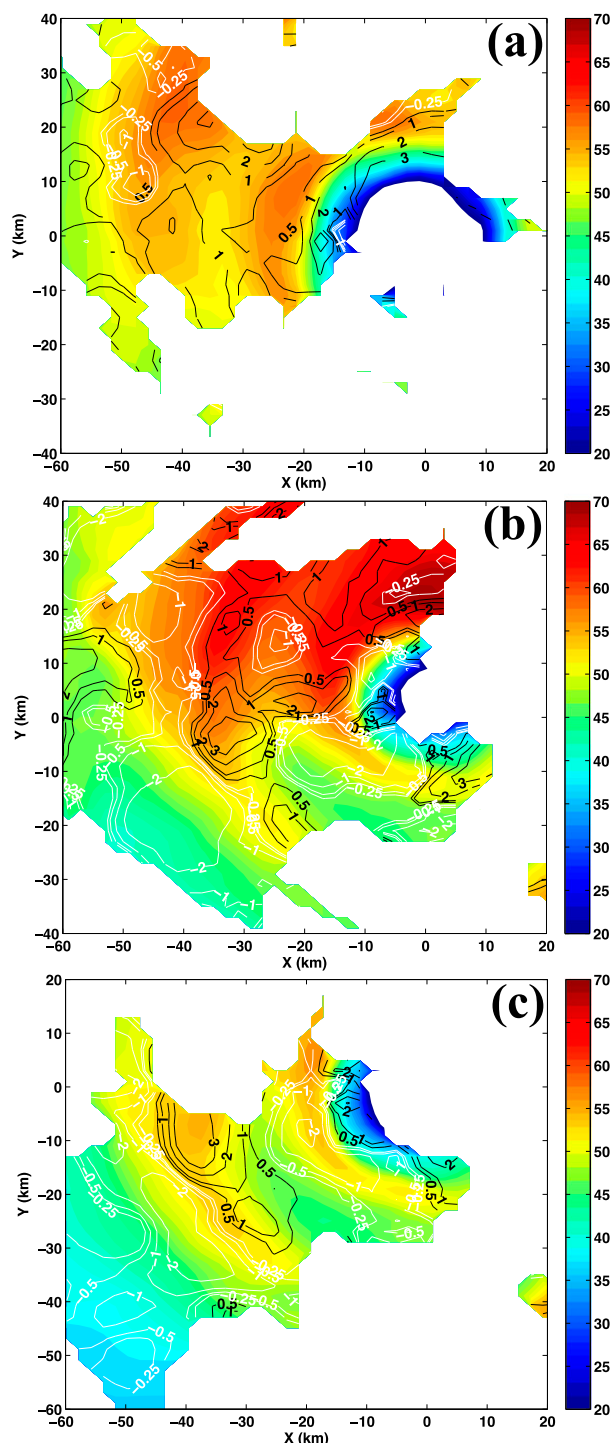


FIG. 5. Horizontal cross sections of total horizontal wind speed (shaded) and vertical velocity (contours) from the P-3 TA radar on 22 Sep 2005 at (a) 1927, (b) 2015, and (c) 2030 UTC. Positive (negative) contours are in black (white).

(see colored lines in Fig. 4 for aircraft tracks), which are coincident with the TA data shown in Fig. 5. The IWRAP data shown here are a representative sample of the larger collection of data during this period.

Figure 6 shows IWRAP data in a vertical cross section at nadir for the 1910–1920 UTC radial leg. The Ku-band reflectivity (Fig. 6a) shows the inner and outer eyewalls at radii of  $\sim 25$  and  $50$  km, respectively, along with thin bands of reflectivity present in the region between the inner and outer eyewalls (mostly between a radius of  $\sim 40$  and  $\sim 45$  km). Note that the region of high reflectivity just below flight level ( $\sim 1.5$  km) is due to issues with the radar digital receiver and only affects reflectivity data at this height outside of heavy precipitation.

Figure 6b shows a comparison of P-3 flight-level wind speed to IWRAP wind speed ( $\sim 1.4$ -km height) as well as SFMR data at the ocean surface. The accuracy statistics for zonal, meridional, and vertical winds for all the legs shown in this section can be found in Figs. 2 and 3. The IWRAP retrievals compare very well with the flight-level data including the ability to capture turbulent perturbations throughout the storm core. A small region of larger wind errors in the IWRAP data can be seen at a radius of  $\sim 36$  km, which is due to a lower SNR (scales inversely with reflectivity) and larger uncertainty in the Doppler velocity. It is apparent that several of the turbulent perturbations captured in the IWRAP data are vertically coherent features that extend from at least  $\sim 1.5$ -km height down to the ocean surface as seen through the correlation of the flight-level, IWRAP, and SFMR data in Fig. 6b. The dashed lines in Fig. 6b connect several perturbations in the flight-level and SFMR data. The connection between perturbations observed at higher altitudes (IWRAP data) and those at the ocean surface (SMFR data) will be analyzed further in section 5.

The indication of vertically coherent perturbations highlighted in Fig. 6b is confirmed in Fig. 6c, which shows the computed IWRAP total horizontal wind speeds in the nadir plane. The IWRAP winds reveal the presence of thin bands of intense winds located most notably in the region between the inner and outer eyewalls, but with signatures inside the inner and outer eyewalls as well. These bands (hereafter called eddies) have an oscillatory structure with wind speed perturbations of  $\sim 10$ – $15$   $\text{m s}^{-1}$  from the background flow and radial wavelengths of  $\sim 1.5$ – $3$  km. The wavelengths of the eddies were estimated by manually examining the peak-to-peak distance, which can introduce some subjectivity, especially when the fields have complicated structure. A more rigorous, objective wavelength calculation for all the legs shown in this section is described in section 5.

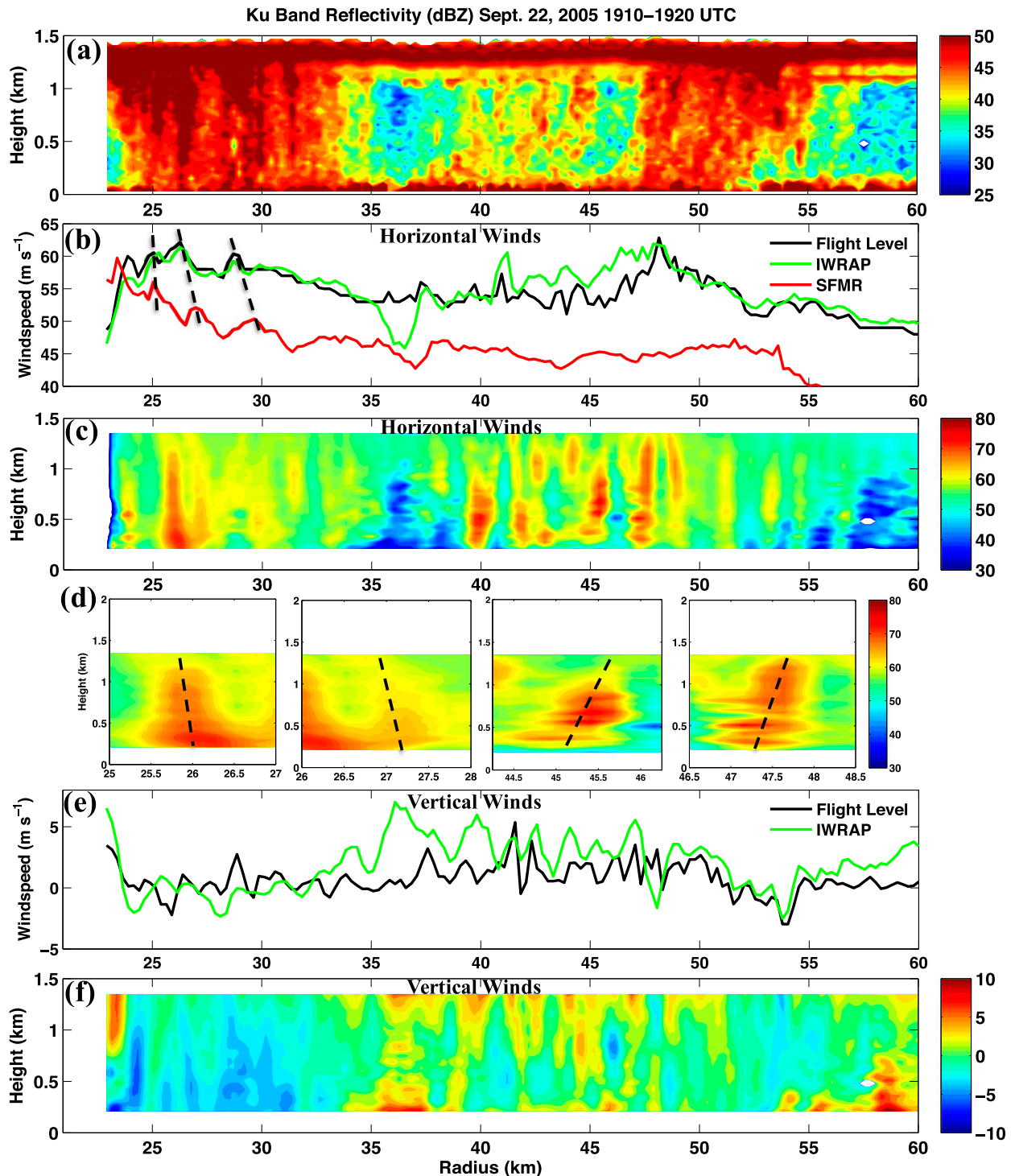


FIG. 6. Vertical cross sections of IWRAP data at nadir between 1910 and 1920 UTC 22 Sep 2005 (black line in Fig. 4) showing (a) Ku-band reflectivity (dBZ), (b) total horizontal wind speed ( $\text{m s}^{-1}$ ) comparison at  $\sim 1.4$ -km height to flight-level data and SFMR data, (c) total horizontal wind speed, (d) zoomed view (one-to-one aspect ratio) of several wind speed features from (c), (e) vertical wind speed ( $\text{m s}^{-1}$ ) comparison to flight-level data, and (f) vertical wind speed. The dashed lines in (b) denote features discussed in the text. The dashed lines in (d) highlight the tilt of the eddies.



The eddies observed in the horizontal winds are largely connected with the reflectivity field in Fig. 6a, especially in the  $\sim 40$ – $45$ -km-radius region. The maximum wind speed in these eddies is  $\sim 75 \text{ m s}^{-1}$  located at or above  $0.5$ -km height, which is  $\sim 7 \text{ m s}^{-1}$  higher than the maximum wind found in the corresponding TA data. This discrepancy is likely due to the IWRAP data having much higher resolution than the TA data. Focusing on individual eddies in Fig. 6d shows a slight tilt radially inward with height in the inner eyewall region (centered at  $26$ - and  $27$ -km radii) and a tilt radially outward with height near the outer eyewall region ( $\sim 45$ - and  $47.5$ -km radii). The tilt in the inner eyewall is consistent with the flight-level and SFMR data shown in Fig. 6b. The tilt structure of the eddies is likely related to the vertical wind shear profiles, which are examined in section 5.

Bell et al. (2012) analyzed dropsonde data in Hurricane Rita during this time period and found the boundary layer height in both the inner and outer eyewalls was at  $\sim 1$  km. The top of the boundary layer was taken to be the height at which the mean radial inflow reduces to 10% of the maximum inflow found near the surface. Other definitions of the boundary layer top have been used, such as the height of the maximum wind speed, which typically results in lower values closer to  $0.5$ -km height (Zhang et al. 2011b). Regardless of the definition, it is clear that the turbulent eddies observed here (Figs. 6b,c,d) extend well above the top of the boundary layer.

Comparisons of flight-level vertical winds to IWRAP-computed vertical winds at  $1.4$  km-height in Fig. 6e reveal a bias of  $-0.68 \text{ m s}^{-1}$  (truth–IWRAP), an RMSE of  $1.86 \text{ m s}^{-1}$  or 115% relative to the truth field, and a correlation coefficient of  $0.60$ . Note that low SNR data, such as the region between  $\sim 35$ - and  $40$ -km radius, have been omitted in these statistics. The quality of the IWRAP vertical velocity estimates are reasonably good in the higher SNR regions, which is where the turbulent eddy activity is prominent.

The computed IWRAP vertical winds in the nadir plane in Fig. 6f reveal oscillations of  $\pm 1$ – $2 \text{ m s}^{-1}$  located most notably in the intermediate region between the inner and outer eyewalls (radius  $\sim 40$ – $50$  km). These vertical wind perturbations are largely in phase with the eddy activity visible in the horizontal winds in Fig. 6c. It is worth noting that no sign of these turbulent eddies is found within the TA data (reflectivity and horizontal/vertical winds), which is not unexpected given the coarse resolution of the analyses. A region of descent in the inner eyewall (radius  $\sim 30$  km) with values from  $\sim -2$  to  $-3 \text{ m s}^{-1}$  is also evident, which is indicative of the decaying inner core described earlier.

Figure 7 shows IWRAP data for the 2000–2010 UTC radial leg, which cut through the most intense portions

of the eyewall (see Figs. 4 and 5b). The Ku-band reflectivity (Fig. 7a) shows the inner and outer eyewall structures of Rita at this time with more attenuation observed than the previous radial leg (Fig. 6a). Comparisons of flight-level total horizontal wind speeds to IWRAP data in Fig. 7b show very good accuracy (discussed in section 2a) in most regions including the very turbulent structure most prominent on the inner edge of the outer eyewall (radius  $\sim 33$ – $40$  km). Note that the larger departure of the IWRAP winds relative to the flight-level winds in Fig. 7b at  $\sim 38$ -km radius is due to minor problems with the data collection. The corresponding SFMR data in the  $\sim 33$ – $40$ -km radial band show signatures of the flight-level eddy activity at the ocean surface observed by comparing the wind perturbations in both datasets. More details on this connection are described in section 5.

The nadir vertical cross section of IWRAP total horizontal wind speeds in Fig. 7c continues to show eddies that are vertically coherent down to  $\sim 200$  m with the peak wind speeds occurring in the  $0.5$ – $1$ -km layer. The most intense eddy activity is at the inner edge of the outer eyewall (radius  $\sim 33$ – $40$  km) with weaker perturbations extending out to  $\sim 55$ -km radius. The inner eyewall also has clear eddy features, but a broader region of elevated winds of  $\sim 70 \text{ m s}^{-1}$  in the  $12$ – $15$ -km-radius region is the main structural feature. Note that gaps in the data from  $\sim 0.5$ -km height and below at radii of  $20$  and  $25$ – $30$  km are due to low SNR data in the weakly precipitating region between the inner and outer eyewalls. Focused images of the eddies in Fig. 7d show mostly similar structure to the previous leg with some tilt radially inward with height in the inner eyewall ( $\sim 16.5$ -km radius) and a more consistent tilt radially outward with height in the outer eyewall ( $\sim 36$ - and  $37.5$ -km radii).

Comparisons of flight-level vertical winds to IWRAP retrievals in Fig. 7e shows a larger bias of  $-1.47 \text{ m s}^{-1}$  and an RMSE of  $2.21 \text{ m s}^{-1}$  or 160% in the higher SNR regions. The large errors in the IWRAP retrievals in the  $\sim 17$ – $30$ -km radius region are due to the low reflectivity signal and are not included in the validation statistics. There are decent correlations between peaks and troughs in both datasets between  $\sim 33$ - and  $\sim 50$ -km radius (correlation coefficient of  $0.67$ ), which is where the turbulent perturbations are dominant. The IWRAP vertical winds in the nadir plane (Fig. 7f) are similar to those in the previous radial leg (Fig. 6f) with oscillations of several meters per second largely in phase with the perturbations in the horizontal wind speeds. A closer look at the phase relationships in horizontal and vertical winds can be found in section 5.

Overall, the characteristics of the turbulent eddies (wavelength, wind speed perturbation, depth, and phasing in horizontal and vertical winds) in the 2000–2010 UTC

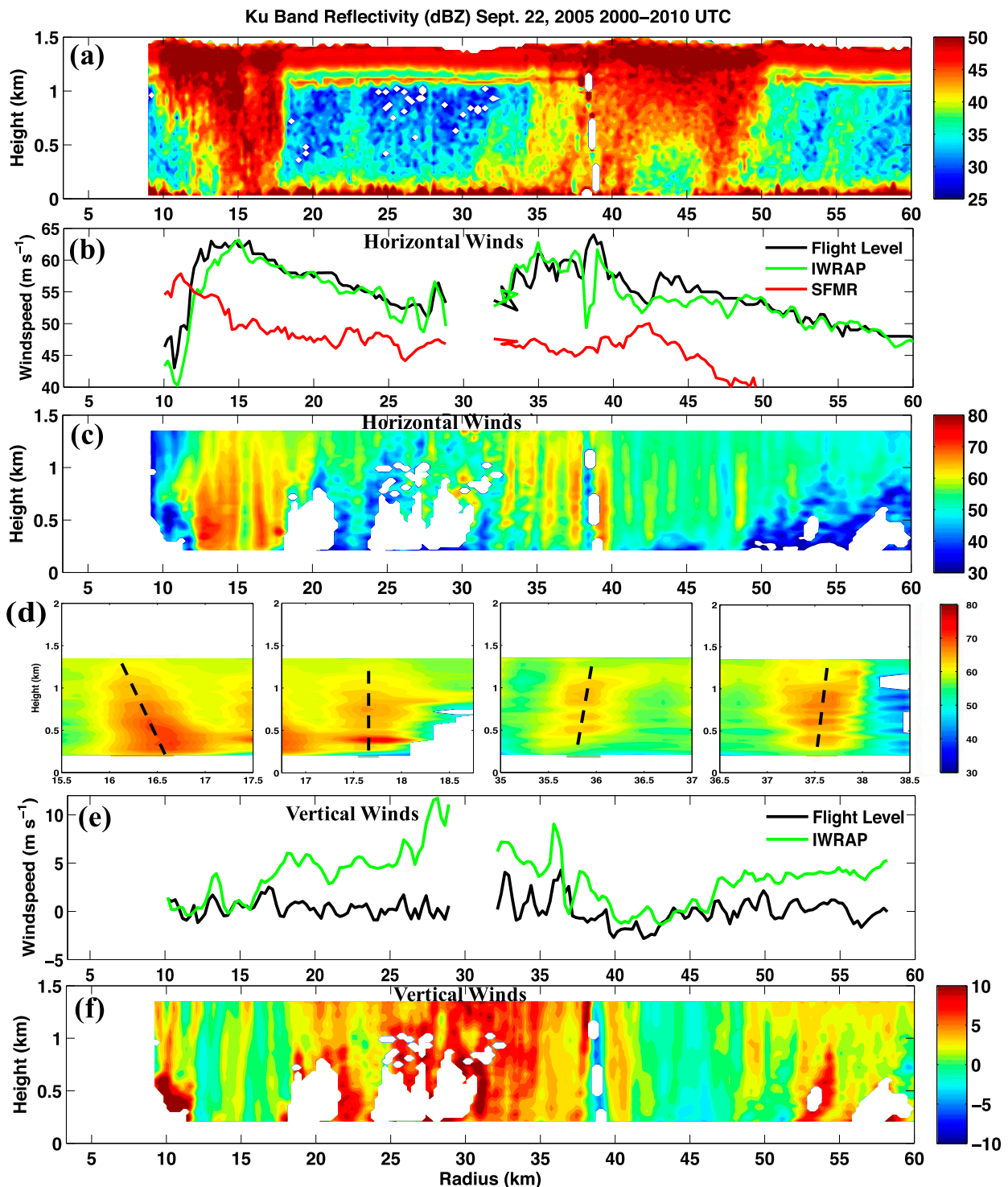


FIG. 7. As in Fig. 6, but between 2000 and 2010 UTC 22 Sep 2005 (blue line in Fig. 4).

radial leg is very similar to the 1910–1920 UTC radial leg. The P-3 TA radar analyses do a better job of capturing the maximum winds in this leg, as the peak wind speeds in the 0.5–1.5-km layer in the TA data

are  $71 \text{ m s}^{-1}$  (Fig. 5b) while the IWRAP maximum winds are  $\sim 75 \text{ m s}^{-1}$  at  $\sim 0.5$ -km height in the inner eyewall. This is due to the larger scale of the maximum wind feature, possibly due to the merging of several

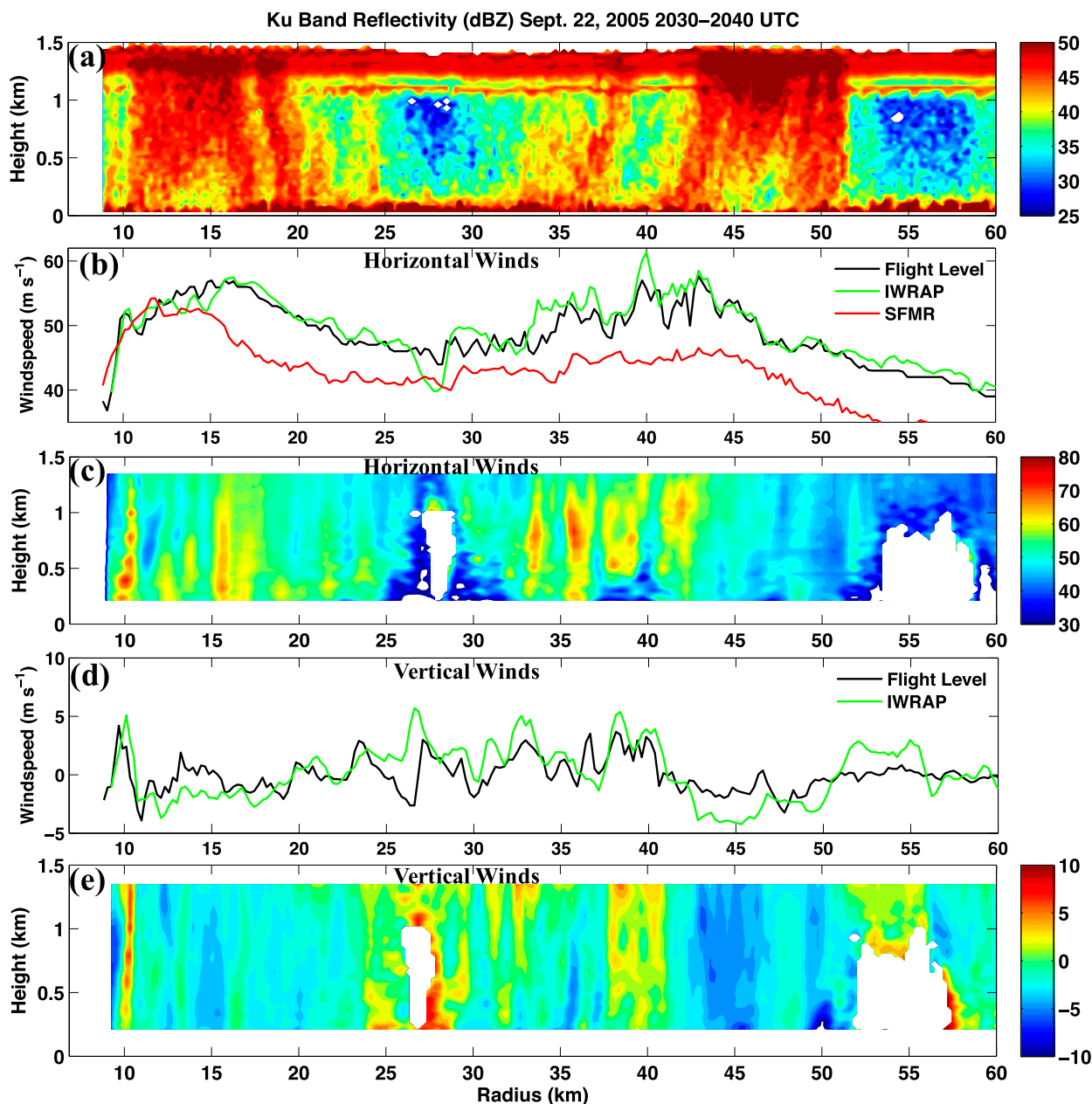


FIG. 8. As in Fig. 6, but between 2030 and 2040 UTC 22 Sep 2005 (red line in Fig. 4), and zoomed images of the wind speed perturbations are not shown.

turbulent eddies, which is slightly resolved by the TA analyses.

Figure 8 shows the final IWRAP radial leg analyzed on this day from 2030 to 2040 UTC, which sampled the southwestern portion of Rita (see Fig. 4). The Ku-band reflectivity (Fig. 8a) again shows the inner and outer eyewall structures clearly with the addition of several thin bands of reflectivity between the inner and outer eyewalls most notably around 35-km radius. As discussed previously, bands of reflectivity originating in the

inner eyewall were observed to propagate both radially and azimuthally in LF radar reflectivity animations (not shown). Portions of these bands are visible in Fig. 4 in the northern and southwestern sections of the inner–outer eyewall transition region, which is sampled by IWRAP in Fig. 8 at ~35-km radius.

Comparisons of flight-level total horizontal wind speeds to IWRAP data in Fig. 8b again show high accuracy (see section 2a for discussion) in most regions including the challenging, highly turbulent structure

most prominent in the transition region ( $\sim 35$ -km radius) and the inner edge of the outer eyewall ( $\sim 40$ -km radius). It was a bit more difficult to visually connect flight-level perturbations with SFMR measurements at the ocean surface in this radial leg, but statistical analysis in section 5 reveals some consistency in the radial wavelength of the perturbations.

The thin reflectivity bands identified in Fig. 8a at  $\sim 35$ -km radius are connected with intense horizontal wind speeds from near flight level to  $\sim 200$  m (Fig. 8c), similar to the previous legs with perturbations from the background flow reaching  $20 \text{ m s}^{-1}$ . The maximum wind speeds are occurring in the 0.5–1-km layer, which is where the top of the boundary layer is typically found. The horizontal (Fig. 8c) and vertical (Fig. 8e) wind speed perturbations are generally in phase, which can be seen more clearly in the inner eyewall (radius of  $\sim 10$ – $15$  km). The IWRAP vertical wind speeds correlate reasonably well with the flight-level data in this pass (Fig. 8d) with a correlation coefficient of 0.62. An IWRAP high bias of  $2.83 \text{ m s}^{-1}$  was found in the original data and that correction has been applied in Figs. 8d and 8e as well as for subsequent analysis of this flight leg. Taking this correction into account, an RMSE of  $1.84 \text{ m s}^{-1}$  or 129% was found for the data in Fig. 8d. Other properties of the turbulent eddies in this pass, such as radial wavelength, are similar to the previous radial legs. Finally, the maximum wind speed found in the TA radar analyses (0.5–1.5-km height) for this leg was  $\sim 57 \text{ m s}^{-1}$ , which is appreciably lower than that found in the IWRAP data ( $\sim 72 \text{ m s}^{-1}$ ).

Although the swath width of IWRAP is small, it is useful to examine the across-track structure of the features described here. Figure 9 shows horizontal cross sections of the storm-relative tangential winds at  $\sim 200$ -m height for the 1910 and 2030 UTC radial legs. In each leg, the vortex-scale mean tangential flow is oriented in the across-track direction, from left to right in Fig. 9a (1910 UTC) and from right to left in Fig. 9b (2030 UTC). The turbulent eddies present in both the inner and outer eyewalls as well as the transition region in Figs. 9a and 9b are stretched in the across-track direction, indicating they are largely aligned with the mean tangential flow. This is consistent with observational studies of roll vortices in the hurricane boundary layer (Wurman and Winslow 1998; Morrison et al. 2005; Lorusso et al. 2008).

#### b. 1700–2200 UTC 23 September

During this time period Hurricane Rita was continuing to weaken, albeit at a slower rate than the previous day [see Fig. 2 in Didlake and Houze (2011) for the intensity time series], as the outer eyewall contracted and

merged with the inner eyewall. Figure 10 shows an LF radar reflectivity scan of Rita ( $\sim 1.5$ -km height) at 1846 UTC 23 September revealing a single eyewall feature with a noteworthy wavenumber-1 structure due to the presence of increasing southwesterly vertical wind shear (Knabb et al. 2006). The P-3 aircraft mounted with IWRAP made several passes through the storm center during this time period with two representative radial legs shown in Fig. 10. Figure 11 shows IWRAP data between 1740 and 1750 UTC, while Fig. 12 shows the 2050–2100 UTC data. Note that the SFMR had data dropouts during these passes and was not useful for the present analysis.

Figure 11a shows a nadir vertical cross section of C-band reflectivity from IWRAP revealing that the inner (radius of  $\sim 30$  km) and outer (radius of  $\sim 40$  km) eyewalls still persist in terms of precipitation at this time, but the intermediate region is very narrow. The C-band reflectivity is shown here to minimize attenuation, but Ku-band Doppler velocities are used for the wind retrievals. Comparisons of flight-level winds to IWRAP data in Fig. 11b show that the maximum winds have a clear peak in the inner eyewall (radius of  $\sim 26$  km) at this time with only a minor increase in the outer eyewall feature (radius of  $\sim 37$  km). The IWRAP total horizontal wind speeds in Fig. 11c shows a broad region of very intense winds ( $\sim 70 \text{ m s}^{-1}$ ) extending from a radius of  $\sim 23$  to  $\sim 33$  km, which is a result of the nearly complete eyewall merging process. Turbulent eddies with similar characteristics to those shown on the previous day are embedded within this region and are also observed in the flight-level winds (between 25- and 30-km radius). The maximum wind speeds induced by these eddies is  $\sim 80$ – $85 \text{ m s}^{-1}$  located between 0.5- and 1-km height at 25-km radius (Fig. 11d).

An interesting observation is that the most intense eddy activity is now located at the inner edge of the inner eyewall feature (merging stage) whereas on the previous day it was located on the inner edge of the outer eyewall feature (concentric stage). This evolution is consistent with an intensifying outer eyewall during the concentric eyewall stage and a reintensification of the inner eyewall during the merging stage. In addition, the tilt of the eddies during the merging stage is largely radially outward with height from the inner to the outer eyewall features (Fig. 11d). During the concentric eyewall stage on 22 September, the eddies were tilted radially outward with height only in the outer, intensifying eyewall with the opposite tilt found in the inner, decaying eyewall. Detailed analysis of this evolution with regard to the instability source for the turbulent eddies is presented in section 5.

The IWRAP vertical wind speeds compare well with flight-level data for this pass (Fig. 11e). Statistics show an IWRAP high bias of  $1.35 \text{ m s}^{-1}$ , RMSE of  $1.88 \text{ m s}^{-1}$

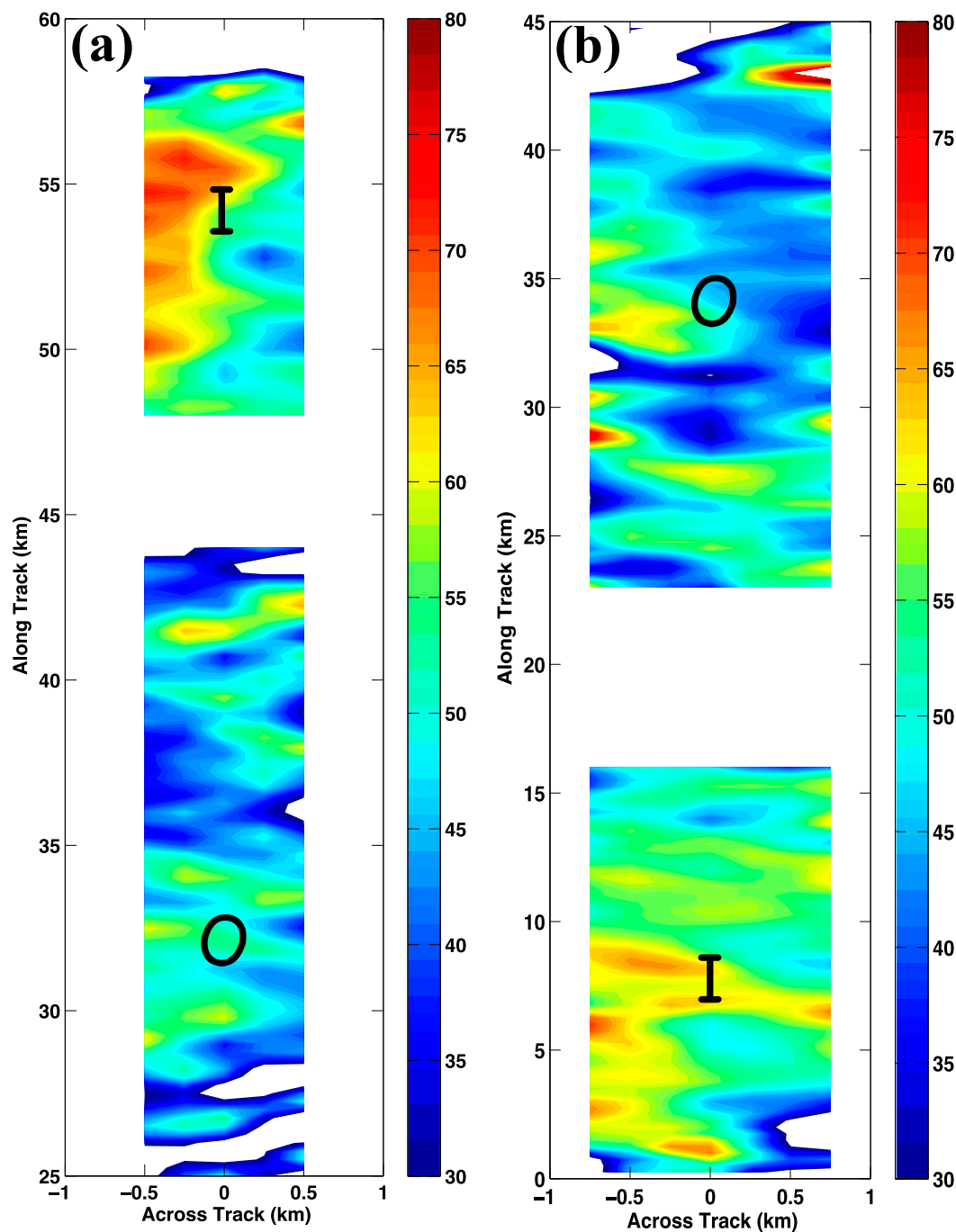


FIG. 9. Horizontal cross sections ( $\sim 200$ -m height) of IWRAP-derived storm-relative tangential winds ( $\text{m s}^{-1}$ ) (a) between 1910 and 1920 UTC and (b) between 2030 and 2040 UTC 22 Sep 2005. The “I” and “O” denote the locations of the inner and outer eyewalls, respectively. The horizontal axis is exaggerated to show detail.

or 110% relative to the truth field, and a correlation coefficient of 0.77. The IWRAP vertical winds in Figs. 11e and 11f show a strong updraft at  $\sim 25$ -km radius, which is collocated with the very intense horizontal wind speeds in Figs. 11c and 11d. Oscillations in the

vertical winds are also clear with wavelengths of  $\sim 3$ – $5$  km, which are slightly larger than the previous day. The vertical winds are, again, largely in phase with the horizontal winds and get progressively weaker moving radially away from the storm center.



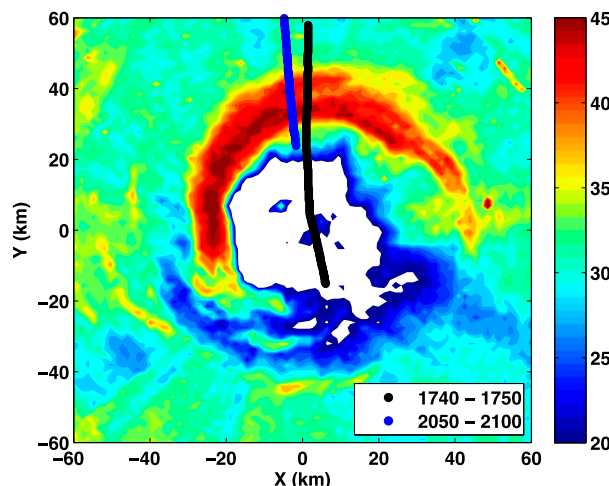


FIG. 10. Horizontal cross section ( $\sim 1.5$ -km height) of radar reflectivity (C band) in Hurricane Rita at  $\sim 1846$  UTC 23 Sep 2005 from the lower-fuselage radar on the NOAA P-3 aircraft. The colored lines denote the flight tracks of the P-3 aircraft on 23 Sep 2005 where IWRAP data are analyzed.

Finally, IWRAP data is shown approximately 3 h later, between 2050 and 2100 UTC, in the northern section of the eyewall in Fig. 12. The Ku-band reflectivity (Fig. 12a) shows a very wide, completely merged eyewall that extends from  $\sim 25$ - to 45-km radius. The thin bands of enhanced reflectivity visible in previous IWRAP radial legs are not as apparent now, but in situ and IWRAP-derived total horizontal wind speeds at flight level (Fig. 12b) continue to show good agreement on the turbulent eddy activity at inner radii ( $\sim 25$ – $35$  km). The vertical cross section of IWRAP total horizontal winds at nadir (Fig. 12c) shows that the most intense eddy activity is located on the inner edge of the merged eyewall ( $\sim 25$ – $30$ -km radius) with these perturbations becoming less intense as the radius increases. These eddies continue to have similar characteristics to the previous radial legs, including radial wavelength, depth, and perturbation intensity.

The IWRAP vertical wind speeds compare reasonably well with flight-level data for this pass (Fig. 12d). When considering data contained in the high-reflectivity region (radius of  $\sim 25$ – $48$  km) the IWRAP high bias is  $1.14 \text{ ms}^{-1}$ , the RMSE is  $1.98 \text{ ms}^{-1}$  or 106%, and the correlation coefficient is 0.62. Beyond  $\sim 48$ -km radius, the SNR of the IWRAP data is lower and the band of high-reflectivity echoes near flight level can cause problems with the fall speed/vertical velocity calculation. The IWRAP vertical winds in Figs. 12d and 12e again show generally consistent phasing between perturbation horizontal and vertical winds, although the radial wavelengths of the vertical winds are not as

clearly defined as the horizontal winds. The most intense vertical winds are located near the inner edge of the merged eyewall ( $\sim 25$ – $30$ -km radius), which is consistent with the horizontal winds.

## 5. Understanding the nature of the turbulent eddies

### a. Objective wavelength detection

Manual inspection of feature wavelengths, which was discussed in section 4, can lead to inaccuracies if the signal is complicated or noisy. To calculate the eddy wavelengths objectively and gain more physical insight into their nature and potential role in the storm evolution, an autocorrelation analysis is performed. The discrete autocorrelation function at lag  $\tau$  can be expressed as

$$R(\tau) = \frac{1}{(n - \tau)\sigma^2} \sum_{i=1}^{n-\tau} (f_i - \bar{f})(f_{i+\tau} - \bar{f}), \quad (5)$$

where  $n$  is the sample size of variable  $f$ ,  $\sigma^2$  is the sample variance, and the overbar is the sample mean. The autocorrelation function is applied to the horizontal wind speed fields shown in section 4 with various spatial lags to determine the structure of oscillations in the data. The spatial lag increment is the horizontal grid spacing of the data (250 m). Figure 13 shows an example autocorrelation function for the 1910–1920 UTC 22 September data using flight-level horizontal wind speed. Two general features are apparent from Fig. 13: 1) a secondary peak in the autocorrelation at a lag of  $\sim 23$  km and 2) several smaller-scale peaks identified at a wide range of spatial lags. The secondary peak in the autocorrelation at  $\sim 23$  km reflects the wavelength of the inner–outer eyewall feature with one maximum in wind speed in the inner eyewall (lag 0) and a secondary maximum in the outer eyewall. The smaller-scale peaks in the autocorrelation reflect the eddies present in the data. The wavelengths of the eddies can be determined by computing the distance between small-scale peaks in the autocorrelation, which produces values between  $\sim 1$  and 3 km with a mean value of 1.97 km.

The wavelengths of the small-scale eddies are computed for each vertical level of IWRAP data and for the SFMR data analyzed in section 4 (five legs for IWRAP and three legs for SFMR). Figure 14 shows histograms of the distribution of wavelengths focusing on features with scales of 10 km or less. The IWRAP data (Fig. 14a) show that the bulk of the eddy wavelengths are contained in the 1–3-km interval with maximum values of  $\sim 6$  km and a mean value of 1.88 km. The SFMR data (Fig. 14b) indicate similar results with most of the eddy wavelengths found in the 1–3-km range, but with maximum values of 9–10 km and a mean value of 2.65 km.

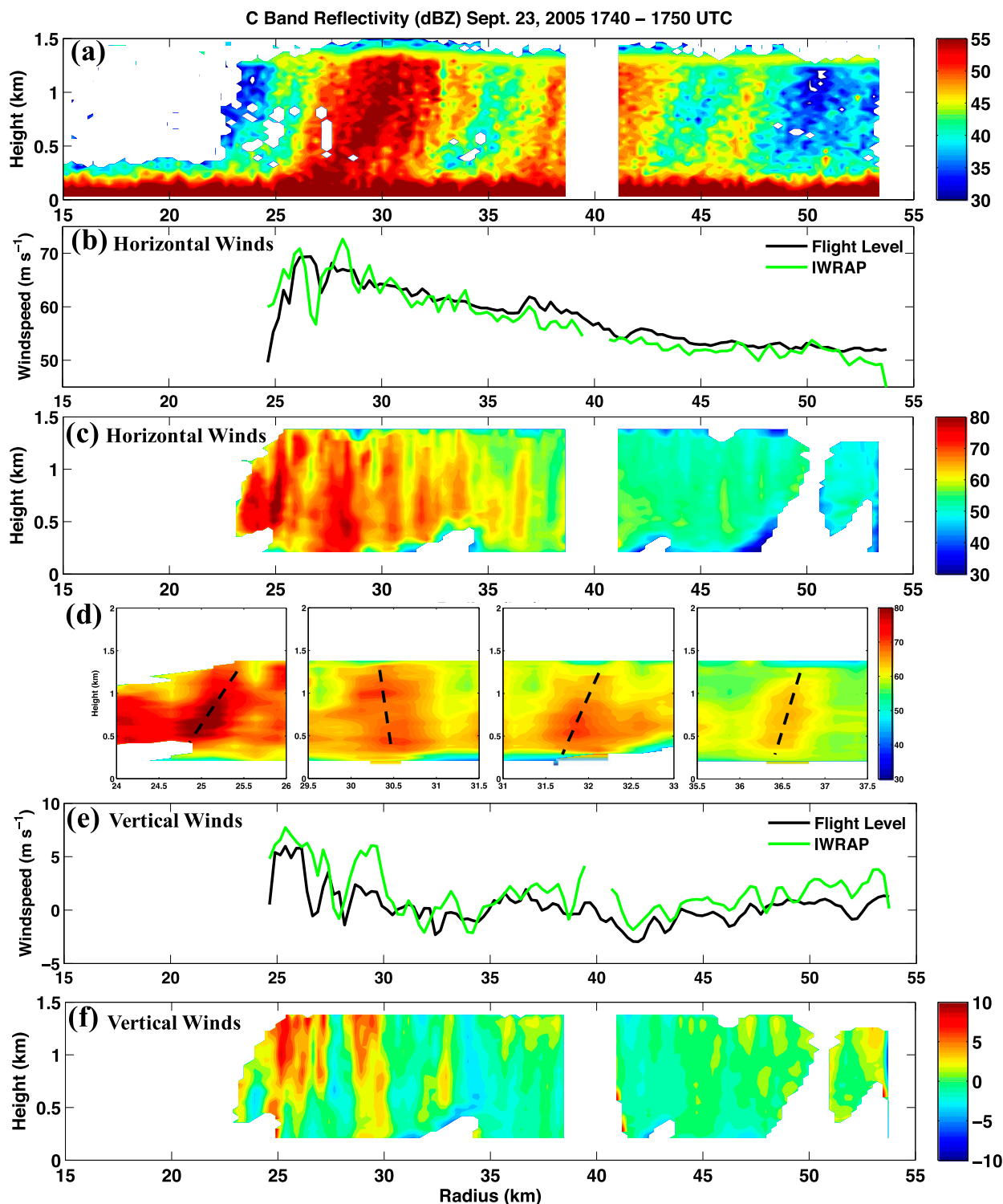


FIG. 11. Vertical cross sections of IWRAP data at nadir between 1740 and 1750 UTC 23 Sep 2005 (black line in Fig. 10) showing (a) C-band reflectivity (dBZ), (b) total horizontal wind speed ( $\text{m s}^{-1}$ ) comparison at  $\sim 1.4$ -km height to flight-level data, (c) total horizontal wind speed ( $\text{m s}^{-1}$ ), (d) zoomed view (one-to-one aspect ratio) of several wind speed features from (c), (e) vertical wind speed ( $\text{m s}^{-1}$ ) comparison at  $\sim 1.4$ -km height to flight-level data, and (f) vertical wind speed ( $\text{m s}^{-1}$ ). The dashed lines in (d) highlight the tilt of the eddies. All IWRAP winds were computed with Ku-band Doppler velocities. Note that SFMR data had dropouts in the eyewall region and were not useful.

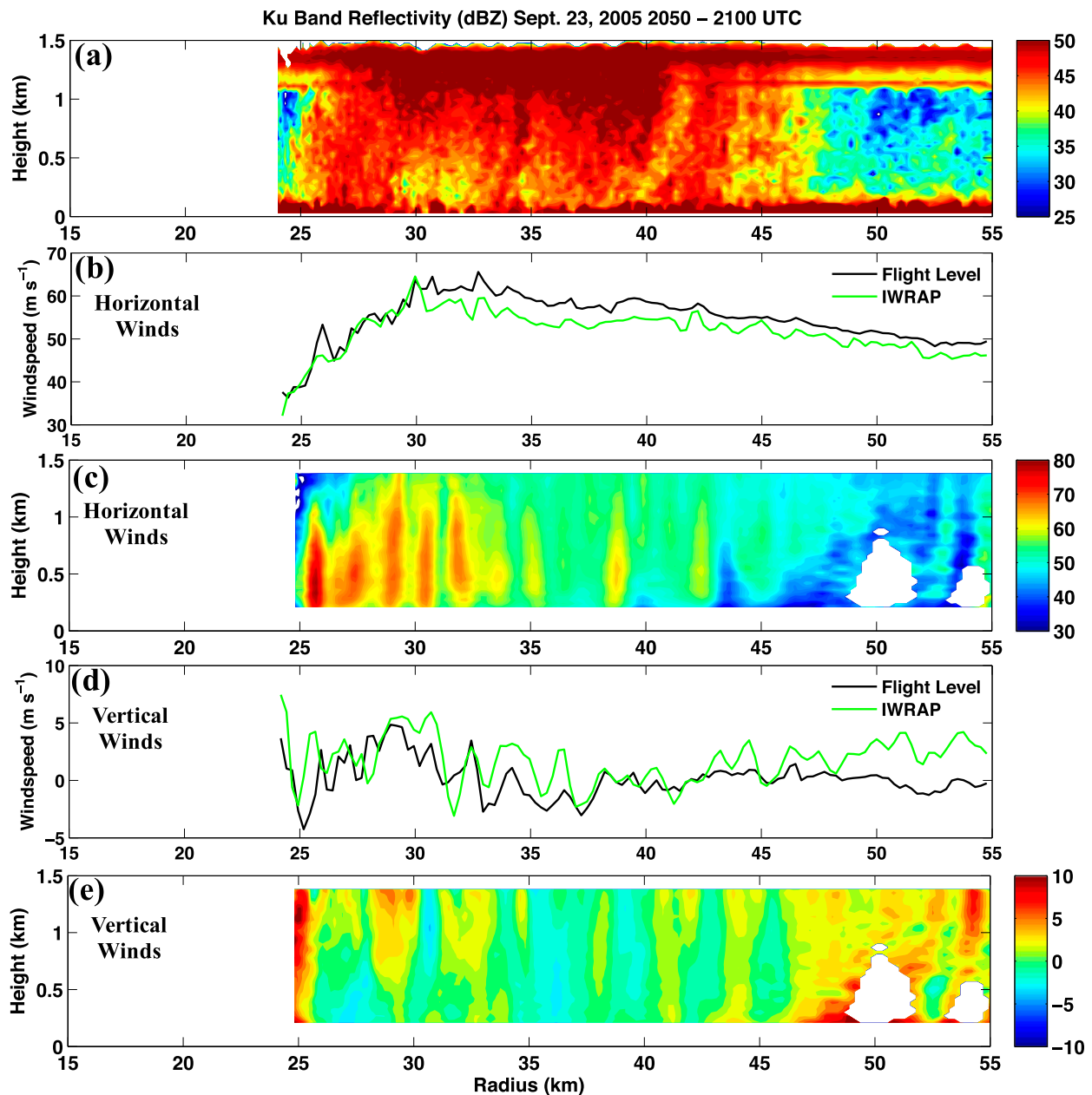


FIG. 12. As in Fig. 11, but between 2050 and 2100 UTC 23 Sep 2005 (blue line in Fig. 10), showing Ku-band reflectivity in (a), and zoomed images of the wind speed perturbations are not shown.

Note that removal of two grid interval scales (500 m) from the data did not significantly change the results described above.

Clearly, the sample sizes between the IWRAP and SFMR data are different. To account for the smaller sample size in the SFMR data, an equivalent sample was constructed with IWRAP by only including data at one vertical level (near flight level where the data coverage was good) and for the same legs where SFMR data were available. The mean eddy wavelength for this IWRAP

sample was 2.58 km, which is consistent with the SFMR data. Other vertical levels were fairly similar because the eddies are generally vertically coherent structures.

The conclusions from this objective wavelength analysis are the following: 1) the turbulent eddies identified in the flight-level and IWRAP data have a mean wavelength of just under 2 km, which is generally consistent with the manual inspection of data described in section 4, and 2) the mean wavelength of perturbations identified in the SFMR data is also  $\sim 2$  km or slightly

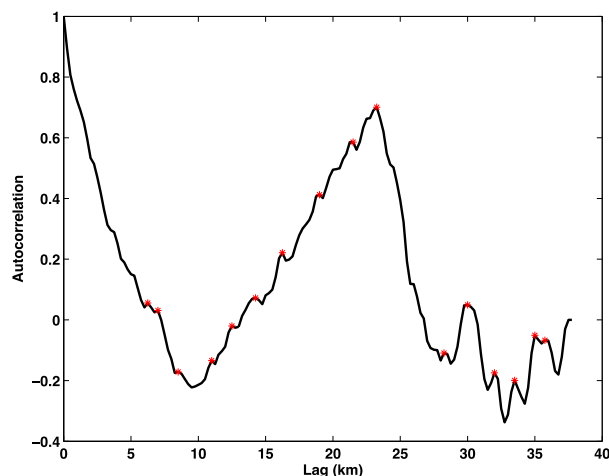


FIG. 13. Autocorrelation function for horizontal wind speed flight-level data between 1910 and 1920 UTC 22 Sep 2005. See Fig. 6b for the flight-level data. The red stars denote the detection of peaks in the autocorrelation.

larger. The presence of slightly larger wavelengths in the SFMR data, relative to IWRAP, is likely due to the larger footprint of the instrument. The consistency between the flight-level, IWRAP, and SFMR wavelengths indicates that the turbulent eddies are vertically coherent features that will have dynamic effects from the ocean surface through the boundary layer and into the free atmosphere.

#### b. Boundary layer rolls or potential vorticity waves?

The ubiquitous presence of turbulent eddies in Hurricane Rita shown in the previous sections is interesting and obvious questions arise: what are these wave-like features and do they play a role in the storm evolution? The eddy characteristics documented and discussed in the previous sections (radial wavelength, perturbation intensity, location, etc.) have some similarities to previous studies on boundary layer roll vortices.

Wurman and Winslow (1998) presented some of the first radar observations of hurricane boundary layer rolls using a mobile Doppler radar that sampled the landfall of Hurricane Fran (1996). They analyzed Doppler velocity data with a range resolution of 75 m and found typical roll wavelengths of  $\sim 600$  m and depths of  $\sim 1$  km with tangential (along roll) and radial (across roll) wind speed variations of  $\sim 20$ – $30$  and  $\sim 3$ – $5$   $\text{m s}^{-1}$ , respectively. Morrison et al. (2005) analyzed perturbation radial velocity data from WSR-88Ds for several hurricane landfalls and found evidence of roll vortices in the boundary layer with average wavelengths, depth, aspect ratio, and residual velocity of  $\sim 1450$  m, 660 m, 2.4, and  $7$   $\text{m s}^{-1}$ , respectively. They used the velocity–azimuth display (VAD) method to compute mean horizontal

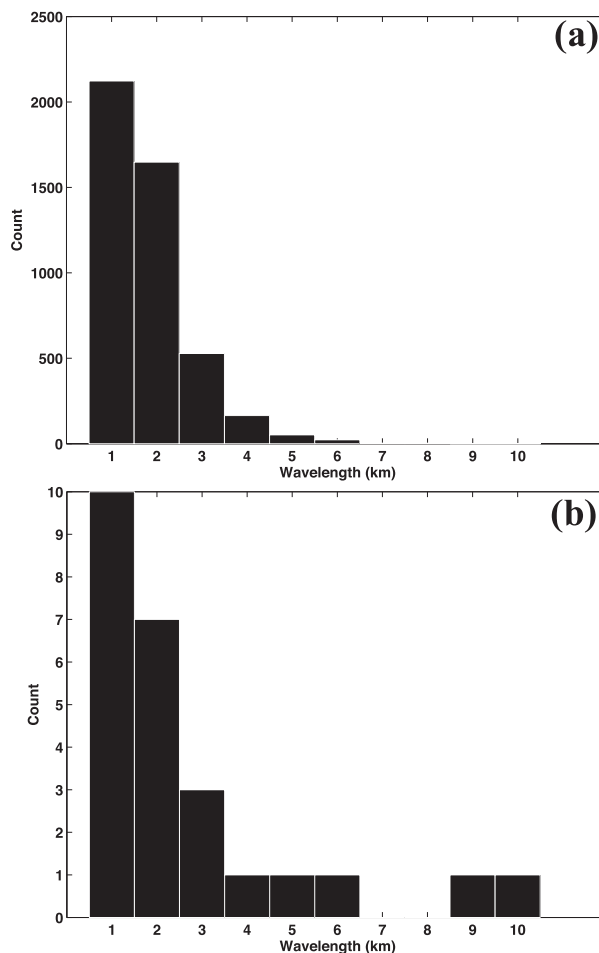


FIG. 14. Histograms of small-scale eddy wavelengths computed using the autocorrelation analysis for (a) IWRAP horizontal wind speed and (b) SFMR horizontal wind speed. See the text for details of the data included in the histograms and analysis methods.

wind vectors over radar scan circles with a range of  $\sim 5$ – $10$  km (typical area  $>100$   $\text{km}^2$ ). These mean winds were subtracted from the total radial velocity field to produce perturbation fields with an average radial and vertical spacing of 250 and  $\sim 25$  m, respectively.

Lorsolo et al. (2008) analyzed mobile Doppler radar observations with a range resolution of 67 m during the landfalls of Hurricane Isabel (2003) and Hurricane Frances (2004) with a similar methodology to Morrison et al. (2005). They found evidence of coherent linear features in the boundary layer with typical wavelengths of  $\sim 200$ – $650$  m, which were well correlated with the near-surface wind field. In addition, Kosiba and Wurman (2014) described 400–500-m-wavelength boundary layer roll circulations using very finescale (20 m) dual Doppler analyses from mobile radar data during the landfall of Hurricane Frances (2004). These roll circulations were shown to induce large vertical fluxes of horizontal

momentum (up to  $12 \text{ m}^2 \text{ s}^{-2}$ ) with substantial variability across the domain, which reflects the importance of 3D measurements.

The Wurman and Winslow (1998), Morrison et al. (2005), Lorsolo et al. (2008), and Kosiba and Wurman (2014) observational results have provided very important characteristics of turbulent structures in the hurricane boundary layer. However, the primary focus on Doppler radial velocities (rather than 3D winds) over small regions [e.g., a  $5.5\text{-km}^2$  horizontal region for Kosiba and Wurman (2014) 3D winds] and the effects of intense surface friction from land and shallow ocean depths complicates the understanding of the structures. The IWRAP observations and 3D wind calculations over the open ocean at high resolution and covering large radial domains represents an important dataset to understand coherent, turbulent eddies in the lower levels of hurricanes.

Studies by Foster (2005) and Nolan (2005) have provided a theoretical understanding of the structure and formation mechanisms of boundary layer rolls in hurricanes. Foster (2005) completed a linear and nonlinear stability analysis of perturbations to the typical mean flow in the hurricane boundary layer. Shear instabilities in the mean vertical profile of tangential and radial velocities were identified as the source for the roll vortices. Nolan (2005) performed a linear stability analysis and nonlinear numerical simulations of axisymmetric hurricane-like vortices and also found that vertical shear of the mean boundary layer flow provides the energy source for finescale bands or roll vortices. Of relevance to the present study, Nolan (2005) also found that the location of the largest wave amplitudes moves radially inward as the inertial stability of the vortex decreases beyond the radius of maximum winds. This may partly explain the movement of the most intense turbulent eddies from the inner edge of the outer eyewall on 22 September to the inner edge of the inner eyewall on 23 September. However, the evolution of the vertical wind shear in the boundary layer is fundamental to the instability and roll generation.

Figure 15 shows the evolution of the mean tangential and radial wind profiles on 22 and 23 September from IWRAP and SFMR data. The SFMR tangential and radial winds are determined by using the IWRAP wind directions at  $\sim 200\text{-m}$  height. The wind profiles in Fig. 15 are averaged in radius over the inner and outer eyewalls with each eyewall incorporating half of the intermediate region between the two eyewall features. For the 2050 UTC leg on 23 September, the merged eyewall is split into two equal portions to represent the inner and outer regions.

During the concentric eyewall stage on 22 September, the outer eyewall profile of tangential and radial winds

(Figs. 15a and 15b) has larger vertical shear than the inner eyewall profile for both the 1910 and 2030 UTC radial legs. The magnitude of the vertical shear of the tangential (radial) wind averaged over height and time is  $8.4 \times 10^{-3}$  ( $1.1 \times 10^{-2}$ )  $\text{s}^{-1}$  for the inner eyewall and  $1.4 \times 10^{-2}$  ( $1.9 \times 10^{-2}$ )  $\text{s}^{-1}$  for the outer eyewall on 22 September. Note that the radial shear values are larger than the tangential shear values in both eyewall features. During the completion of the eyewall replacement process on 23 September, the largest vertical shear shifts to the inner portion of the eyewall shown by the tangential (Fig. 15c) and radial (Fig. 15d) wind profiles at 1740 and 2050 UTC. The magnitude of the vertical shear of the tangential (radial) wind averaged over height and time is  $1.7 \times 10^{-2}$  ( $2.2 \times 10^{-2}$ )  $\text{s}^{-1}$  for the inner eyewall and  $8.6 \times 10^{-3}$  ( $1.4 \times 10^{-2}$ )  $\text{s}^{-1}$  for the outer eyewall on 23 September. The peak vertical shear values are generally larger during the merging stage than those found during the concentric stage, and the radial shear is dominant during both stages.

These findings are consistent with the most intense turbulent eddy activity shifting from the inner edge of the outer eyewall on 22 September to the inner edge of the inner eyewall on 23 September. On 22 September, the outer eyewall was contracting and intensifying with stronger radial inflow in the boundary layer than in the inner, decaying eyewall. On 23 September, the outer eyewall had merged with the inner eyewall resulting in an increase (decrease) of tangential winds at inner (outer) radii. In addition, the radial inflow in the low-level boundary layer increased dramatically in the inner eyewall along with radial outflow occurring in the upper portions of the boundary layer and into the free atmosphere.

The tilt of the turbulent eddies identified in section 4 follows the evolution of the radial wind shear discussed above. During the concentric eyewall stage, the eddies in the outer eyewall generally tilted radially outward with height (Figs. 6d and 7d), which is consistent with stronger low-level inflow and vertical shear of the radial wind (Fig. 15b). In the inner eyewall, the eddies generally tilted radially inward with height (Figs. 6d and 7d), collocated with weaker radial inflow and vertical shear (Fig. 15b). However, the inner eyewall tilt does not appear to fully reflect the radial flow structure. There may be additional factors affecting the tilt, such as the interaction of the eddies with the mean flow. During the merging eyewall stage, the eddies are generally tilted radially outward with height at all radii (Fig. 11d), which is consistent with a large increase in the radial inflow and vertical shear at inner radii (Fig. 15d).

Despite the similarities of the data presented here to previous studies of boundary layer rolls, there are



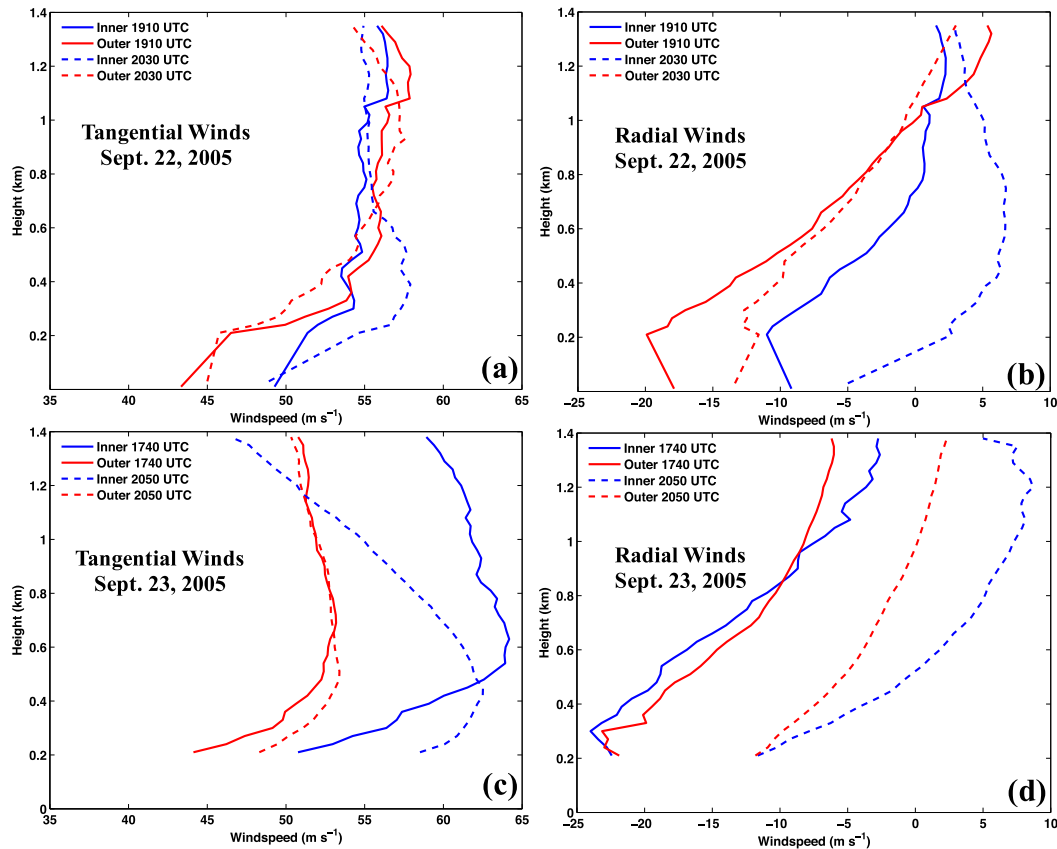


FIG. 15. Vertical profiles of storm-relative tangential and radial winds from IWRAP and SFMR data averaged over the inner and outer eyewall features of Rita on 22 and 23 Sep 2005. (a),(c) Tangential and (b),(d) radial winds on (a),(b) 22 and (c),(d) 23 Sep. The SFMR winds on 22 Sep are located at 10-m height with linear interpolation to the lowest IWRAP level of  $\sim 200$  m. See text for more details.

notable differences. The wavelengths of the features described in this paper are generally larger than those documented in previous studies, which could be due to the effects of strong surface friction from land influences and very shallow ocean depths in the prior studies. The majority of the turbulent eddies shown in this paper extend from the ocean surface up to at least 1.5-km height (flight level) with similar finescale bands observed by IWRAP in Hurricane Isabel (2003) up to at least 2.0-km height (Guimond et al. 2014). These observations are clearly above the top of the boundary layer in these storms and there are no obvious reasons why they should not extend to higher altitudes, especially if the eddies are coupled to the vertical velocity field.

Substantial coupling of the horizontal and vertical winds was noted in each radial leg of data described in section 4. To examine this coupling more closely, the eddy momentum fluxes ( $v'w'$ ,  $u'w'$ , and  $v'u'$ ) were computed and IWRAP fields for the 2030–2040 UTC 22 September leg are shown in Fig. 16. Perturbations were defined as fluctuations from the low-pass-filtered

wind components across the radial leg. The filter (running mean) was applied in the forward and backward directions to enable zero phase shift with a cutoff wavelength of  $\sim 5$  km, which encompasses nearly all the eddy wavelengths detected in the IWRAP data (Fig. 14a). Storm motion is also removed from the perturbation winds.

Figure 16a shows the IWRAP radial profile of the vertical flux of tangential momentum  $v'w'$  averaged over two vertical layers, lower ( $\sim 0.2$ – $0.5$  km) and upper ( $\sim 0.5$ – $1.0$  km). Note that Fig. 16 shows the natural logarithm of the eddy fluxes, but here raw values are discussed. In the inner eyewall, peak eddy momentum flux values are  $\sim 55 \text{ m}^2 \text{ s}^{-2}$  or larger in two narrow regions centered at radii of  $\sim 10$  and  $16$  km extending through the full depth of the two vertical layers. The locations of these large positive momentum fluxes are coincident with the eddies identified in Fig. 8 and discussed in section 4. There are several other regions of positive as well as negative eddy fluxes in the inner and outer eyewalls. The mean momentum flux over the inner eyewall

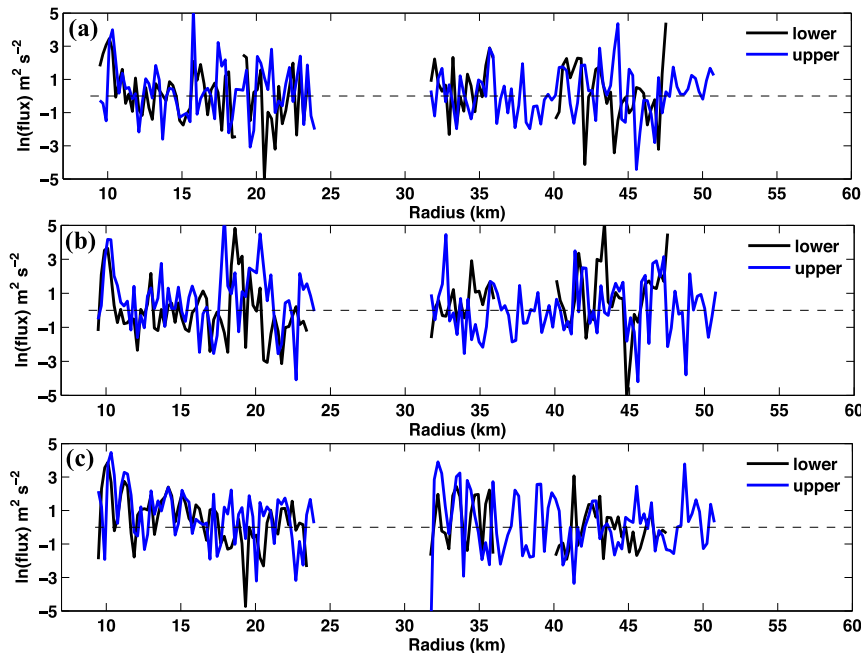


FIG. 16. Radial profiles of IWRAP eddy momentum fluxes between 2030 and 2040 UTC 22 Sep 2005 for two vertical layers. The natural logarithm of the fluxes (retaining signs) is shown to accommodate the large range in values. (a) The vertical flux of tangential momentum  $[\ln(v'w')]$ , (b) the vertical flux of radial momentum  $[\ln(u'w')]$ , and (c) the radial flux of tangential momentum  $[\ln(v'u')]$ . The “lower” layer is fluxes averaged between  $\sim 0.2$ - and  $0.5$ -km height, and the “upper” layer is fluxes averaged between  $\sim 0.5$ - and  $1.0$ -km height. Note that the radii of maximum winds for the inner and outer eyewalls is  $\sim 15$  and  $\sim 40$  km, respectively.

(radius  $< 30$  km) in Fig. 16a is  $\sim 1.5 \text{ m}^2 \text{ s}^{-2}$  for both the lower and upper layers. In the outer eyewall (radius  $> 30$  km), the mean momentum flux is  $\sim 1.5 \text{ m}^2 \text{ s}^{-2}$  and  $0.5 \text{ m}^2 \text{ s}^{-2}$  in the lower and upper layers, respectively. In addition, at radii of  $\sim 36$  and  $41$  km in the outer eyewall, instantaneous momentum flux values of  $10$ – $15 \text{ m}^2 \text{ s}^{-2}$  are found collocated with eddies previously identified in Fig. 8.

Figure 16b shows the radial profile of the vertical flux of radial momentum  $u'w'$ . An intense turbulent eddy located at a radius of  $10$  km is responsible for large vertical fluxes of radial momentum ( $\sim 50 \text{ m}^2 \text{ s}^{-2}$ ) in both layers, which is collocated with large vertical fluxes of tangential momentum ( $\sim 50 \text{ m}^2 \text{ s}^{-2}$ ; Fig. 16a). Peak  $u'w'$  magnitudes reach up to  $150 \text{ m}^2 \text{ s}^{-2}$  located in both the inner and outer eyewalls extending through the depth of the boundary layer ( $< 1.0$  km). The mean momentum flux over the inner eyewall in Fig. 16b is  $\sim 1$ – $3 \text{ m}^2 \text{ s}^{-2}$  with values that get larger with height. In the outer eyewall, the mean momentum fluxes are zero or very slightly negative ( $-0.16 \text{ m}^2 \text{ s}^{-2}$ ) in the lower and upper layers. The vertical fluxes of horizontal momentum calculated here are generally similar to those found in Morrison et al. (2005) and Zhang et al. (2011a),

although the values in some of the eddies appear significantly higher than these studies.

Finally, Fig. 16c shows the radial flux of tangential momentum  $v'u'$ . The structure of  $v'u'$  is generally similar to  $u'w'$  and  $v'w'$  with large positive values located in the turbulent eddies including instantaneous values approaching  $100 \text{ m}^2 \text{ s}^{-2}$  in the intense eddy at  $10$ -km radius. Note that the radius of maximum winds for the inner and outer eyewalls is  $\sim 15$  and  $\sim 40$  km, respectively. Mean fluxes in the inner eyewall range from  $\sim 3$  to  $5 \text{ m}^2 \text{ s}^{-2}$  with smaller values of  $\sim 1$ – $3 \text{ m}^2 \text{ s}^{-2}$  in the outer eyewall. The structure of the momentum fluxes for the turbulent eddies described for the 2030–2040 UTC radial leg is generally representative of other time periods, at least for the concentric eyewall stage. This is consistent with the observation that the horizontal and vertical wind perturbations were in phase for most of the eddies discussed in section 4. Also note that the minimum detectable wavelength with the present data is  $500$  m and the total momentum fluxes may be underestimated because of the effects of very small-scale eddies.

The following physical interpretation emerges from the eddy momentum flux analysis. In both the inner and outer eyewall regions, the vertical flux of tangential

momentum is dominated by positive values at all levels, indicating that the turbulent eddies are lifting high-momentum air upward to the top of the boundary layer and into the free atmosphere. The vertical flux of radial momentum is also typically positive in many of the turbulent eddies throughout the boundary layer. *The sign and structure of the eddy momentum fluxes in this work are in stark contrast to studies of boundary layer rolls, where high-momentum air is transported downward toward the surface and low-momentum air is lifted upward ( $v'w'$  and  $u'w' < 0$ ; Wurman and Winslow 1998; Foster 2005; Morrison et al. 2005).* In addition, the turbulent eddies in the inner eyewall are transporting elevated tangential momentum radially outward ( $v'u' > 0$ ), with signatures of this effect observed out to the inner edge of the outer eyewall.<sup>1</sup>

The positive eddy momentum fluxes discussed above may have some connections to vortex Rossby waves or more generally, potential vorticity waves (e.g., Guinn and Schubert 1993; Montgomery and Kallenbach 1997; Schubert et al. 1999). As mentioned previously, Didlake and Houze (2011) showed strong coupling between perturbations in vorticity and vertical velocity using ELDORA radar observations in Hurricane Rita (2005). They suggested these observations may be connected to vortex Rossby waves with wavelengths of 6–10 km. While vortex Rossby waves have generally larger wavelengths than those documented in this study, it is possible that breaking potential vorticity waves coupled with shear instabilities in the boundary layer may produce smaller wavelengths and intense turbulent fluctuations in the flow field as described here.

## 6. Summary and conclusions

Airborne Doppler radar measurements from the Imaging Wind and Rain Airborne Profiler (IWRAP) as well as other remote sensing and in situ data collected in Hurricane Rita (2005) on 22 and 23 September show the turbulent evolution of an eyewall replacement cycle. These measurements and 3D wind vector calculations reveal the structure of coherent turbulent eddies in the boundary layer (ocean surface up to  $\sim 1.5$  km) of the storm with unprecedented resolution (grid spacing of 250 m in the horizontal and 30 m in the vertical).

The typical characteristics of the turbulent eddies were found to be the following: radial wavelengths of

$\sim 1$ –3 km (mean value is  $\sim 2$  km), depths from the ocean surface (using SFMR data) up to flight level ( $\sim 1.5$  km), aspect ratio of  $\sim 1.3$ , and horizontal wind speed perturbations of  $10$ – $20 \text{ m s}^{-1}$ . The maximum wind speeds found in Hurricane Rita are  $\sim 85$ – $90 \text{ m s}^{-1}$  located in the eddies in the  $0.5$ – $1$ -km layer. The turbulent eddies are aligned parallel to the mean tangential flow, and horizontal velocity perturbations are in phase with vertical velocity perturbations as well as the reflectivity field, indicating the presence of a convectively coupled wave feature. The substantial coupling of the features to convective fields such as vertical velocity and reflectivity (a function of moisture) likely helps to stretch the eddies well above the boundary layer. These characteristics have several similarities to boundary layer roll vortices, although the deeper vertical extent and smaller aspect ratio described here are unique aspects.

The most intense turbulence activity was located on the inner edge of the outer eyewall during the concentric eyewall stage (22 September) with a shift to the inner eyewall during the merging stage (23 September). Theoretical studies of boundary layer rolls and finescale bands by Foster (2005) and Nolan (2005) identified shear instability in the lower-level velocity profile as the energy source for the turbulence. Analysis of the vertical shear of the tangential and radial winds from IWRAP data showed that the most intense turbulence activity was correlated with the strongest vertical wind shear, for which the radial component had the largest values. During the concentric eyewall stage, the outer eyewall is intensifying with a deep layer of inflow and a spinup of the lower-level tangential winds leading to larger vertical gradients in velocity. The inner eyewall is decaying because of opposite arguments leading to weaker vertical gradients in velocity. As the eyewall replacement process evolves to the merging stage, the inner eyewall begins to intensify, with IWRAP finding stronger tangential flow and larger vertical gradients in velocities relative to the outer portions.

Detailed analysis of the eddy momentum fluxes ( $v'w'$ ,  $u'w'$ , and  $v'u'$ ) reveals the upward transport of high-momentum air (flux sign is positive) in the turbulent structures with very large values sometimes approaching  $150 \text{ m}^2 \text{ s}^{-2}$ . This configuration is in contrast to boundary layer roll theory and observations, which show transports of high-momentum air downward toward the surface (flux sign is negative). During the concentric eyewall stage, the turbulent eddies were also transporting elevated tangential momentum radially outward from the inner eyewall extending to the inner edge of the outer eyewall. These characteristics suggest some connections to potential vorticity waves (e.g., Guinn and Schubert 1993;

<sup>1</sup> It is important to consider the gradient of the mean flow when interpreting the eddy momentum fluxes. While some of the eddy momentum flux signatures shown here indicate upgradient transport, a more detailed analysis of the wave–mean flow dynamics is necessary and will be presented in a future study.

Montgomery and Kallenbach 1997; Schubert et al. 1999).

It is possible that breaking potential vorticity waves are coupled to the shear instability present in the boundary layer to produce the turbulent eddies described here. However, more analysis and additional cases are needed to study this hypothesis further.

The IWRAP measurements and retrievals presented in this paper as well as those from a larger collection of data dating back to 2003 represents a new dataset for the hurricane community. The 3D vector wind retrievals presented here validate very well with in situ flight-level data. The zonal (meridional) wind speeds were found to have RMSEs of 3.95 (4.56)  $\text{m s}^{-1}$ , which is  $\sim 10\%$ – $12\%$  of the sampled wind speed, and correlation coefficients of 0.99. For the specific flight legs presented in this paper, the errors are lower ( $\sim 8\%$ – $10\%$ ). The vertical wind speed is a more difficult component to measure/calculate and was evaluated on a leg-by-leg basis. The statistics generally show an RMSE of  $1.94 \text{ m s}^{-1}$  or 124% and a correlation coefficient of 0.65, which allows a reasonably accurate characterization of the turbulent eddies. Other examples and validation of IWRAP data can be found in Guimond et al. (2014).

Coherent turbulence has the ability to play an important role in the intensity and structure change of hurricanes through the transport of momentum, moisture, and heat in the boundary layer and into the bulk vortex aloft. These new observations from IWRAP should be very useful for characterizing the momentum fluxes in hurricanes and evaluating boundary layer parameterizations in numerical models. Fundamental research on eyewall replacement cycles and the role of turbulence in the mean flow evolution can be conducted with the IWRAP dataset, and future work will address this problem in conjunction with numerical models.

**Acknowledgments.** We thank the University of Massachusetts Amherst Microwave Remote Sensing Laboratory for its engineering efforts. The first author thanks Dr. Paul Reasor for discussions on this work. Author Guimond was partially supported by the NASA Weather and Atmospheric Dynamics program (Grant NNH16ZDA001N-WEATHER) directed by Ramesh Kakar. Coauthor Zhang was funded through NOAA Grant NA14NWS4680028. The NASA Ocean Vector Winds Science Team and the NOAA/NESDIS/Center for Satellite Applications and Research Ocean Remote Sensing program provided support for IWRAP research flights and coauthors Sapp and Frasier. Finally, we thank two anonymous reviewers and Ralph Foster for their valuable comments that improved the quality of this paper.

## REFERENCES

- Bell, M. M., and M. T. Montgomery, 2008: Observed structure, evolution, and potential intensity of category 5 Hurricane Isabel (2003) from 12 to 14 September. *Mon. Wea. Rev.*, **136**, 2023–2046, <https://doi.org/10.1175/2007MWR1858.1>.
- , —, and W.-C. Lee, 2012: An axisymmetric view of concentric eyewall evolution in Hurricane Rita (2005). *J. Atmos. Sci.*, **69**, 2414–2432, <https://doi.org/10.1175/JAS-D-11-0167.1>.
- Black, P. G., and Coauthors, 2007: Air–sea exchange in hurricanes: Synthesis of observations from the coupled boundary layer air–sea transfer experiment. *Bull. Amer. Meteor. Soc.*, **88**, 357–374, <https://doi.org/10.1175/BAMS-88-3-357>.
- Bryan, G. H., 2012: Effects of surface exchange coefficients and turbulence length scales on the intensity and structure of numerically simulated hurricanes. *Mon. Wea. Rev.*, **140**, 1125–1143, <https://doi.org/10.1175/MWR-D-11-00231.1>.
- , and R. Rotunno, 2009: The maximum intensity of tropical cyclones in axisymmetric numerical model simulations. *Mon. Wea. Rev.*, **137**, 1770–1789, <https://doi.org/10.1175/2008MWR2709.1>.
- Didlake, A. C. Jr., and R. A. Houze Jr., 2011: Kinematics of the secondary eyewall observed in Hurricane Rita (2005). *J. Atmos. Sci.*, **68**, 1620–1636, <https://doi.org/10.1175/2011JAS3715.1>.
- Emanuel, K. A., 1986: An air–sea interaction theory for tropical cyclones. Part I: Steady-state maintenance. *J. Atmos. Sci.*, **43**, 585–604, [https://doi.org/10.1175/1520-0469\(1986\)043<0585:AASITF>2.0.CO;2](https://doi.org/10.1175/1520-0469(1986)043<0585:AASITF>2.0.CO;2).
- , 1995: Sensitivity of tropical cyclones to surface exchange coefficients and a revised steady-state model incorporating eye dynamics. *J. Atmos. Sci.*, **52**, 3969–3976, [https://doi.org/10.1175/1520-0469\(1995\)052<3969:SOTCTS>2.0.CO;2](https://doi.org/10.1175/1520-0469(1995)052<3969:SOTCTS>2.0.CO;2).
- Fernandez, D. E., E. M. Kerr, A. Castells, J. R. Carswell, S. J. Frasier, P. S. Chang, P. G. Black, and F. D. Marks, 2005: IWRAP: The Imaging Wind and Rain Airborne Profiler for remote sensing of the ocean and the atmospheric boundary layer within tropical cyclones. *IEEE Trans. Geosci. Remote Sens.*, **43**, 1775–1787, <https://doi.org/10.1109/TGRS.2005.851640>.
- Foster, R. C., 2005: Why rolls are prevalent in the hurricane boundary layer. *J. Atmos. Sci.*, **62**, 2647–2661, <https://doi.org/10.1175/JAS3475.1>.
- Franklin, J. L., M. L. Black, and K. Valde, 2003: GPS dropwindsonde wind profiles in hurricanes and their operational implications. *Wea. Forecasting*, **18**, 32–44, [https://doi.org/10.1175/1520-0434\(2003\)018<0032:GDWPIH>2.0.CO;2](https://doi.org/10.1175/1520-0434(2003)018<0032:GDWPIH>2.0.CO;2).
- Gall, R., J. Franklin, F. Marks, E. N. Rappaport, and F. Toepfer, 2013: The Hurricane Forecast Improvement Project. *Bull. Amer. Meteor. Soc.*, **94**, 329–343, <https://doi.org/10.1175/BAMS-D-12-00071.1>.
- Gamache, J. F., 1997: Evaluation of a fully three-dimensional variational Doppler analysis technique. Preprints, *28th Conf. on Radar Meteorology*, Austin, TX, Amer. Meteor. Soc., 422–423.
- , F. D. Marks, and F. Roux, 1995: Comparison of three airborne Doppler sampling techniques with airborne in situ wind observations in Hurricane Gustav (1990). *J. Atmos. Oceanic Technol.*, **12**, 171–181, [https://doi.org/10.1175/1520-0426\(1995\)012<0171:COTADS>2.0.CO;2](https://doi.org/10.1175/1520-0426(1995)012<0171:COTADS>2.0.CO;2).
- Gao, K., and I. Ginis, 2016: On the equilibrium-state roll vortices and their effects in the hurricane boundary layer. *J. Atmos. Sci.*, **73**, 1205–1222, <https://doi.org/10.1175/JAS-D-15-0089.1>.
- , —, J. D. Doyle, and Y. Jin, 2017: Effects of boundary layer roll vortices on the development of an axisymmetric tropical



- cyclone. *J. Atmos. Sci.*, **74**, 2737–2758, <https://doi.org/10.1175/JAS-D-16-0222.1>.
- Guimond, S. R., L. Tian, G. M. Heymsfield, and S. J. Frasier, 2014: Wind retrieval algorithms for the IWRAP and HIWRAP airborne Doppler radars with applications to hurricanes. *J. Atmos. Oceanic Technol.*, **31**, 1189–1215, <https://doi.org/10.1175/JTECH-D-13-00140.1>.
- Guinn, T. A., and W. H. Schubert, 1993: Hurricane spiral bands. *J. Atmos. Sci.*, **50**, 3380–3403, [https://doi.org/10.1175/1520-0469\(1993\)050<3380:HSB>2.0.CO;2](https://doi.org/10.1175/1520-0469(1993)050<3380:HSB>2.0.CO;2).
- Keper, J. D., 2012: Choosing a boundary layer parameterization for tropical cyclone modeling. *Mon. Wea. Rev.*, **140**, 1427–1445, <https://doi.org/10.1175/MWR-D-11-00217.1>.
- Klotz, B. W., and E. W. Uhlhorn, 2014: Improved stepped frequency microwave radiometer tropical cyclone surface winds in heavy precipitation. *J. Atmos. Oceanic Technol.*, **31**, 2392–2408, <https://doi.org/10.1175/JTECH-D-14-00028.1>.
- Knabb, R. D., D. P. Brown, and J. R. Rheme, 2006: Tropical cyclone report: Hurricane Rita 18–26 September 2005. National Hurricane Center Rep., 33 pp., [http://www.nhc.noaa.gov/data/tcr/AL182005\\_Rita.pdf](http://www.nhc.noaa.gov/data/tcr/AL182005_Rita.pdf).
- Kosiba, K. A., and J. Wurman, 2014: Finescale dual-Doppler analysis of hurricane boundary layer structures in Hurricane Frances (2004) at landfall. *Mon. Wea. Rev.*, **142**, 1874–1891, <https://doi.org/10.1175/MWR-D-13-00178.1>.
- Lee, W.-C., P. Dodge, F. D. Marks, and P. H. Hildebrand, 1994: Mapping of airborne Doppler radar data. *J. Atmos. Oceanic Technol.*, **11**, 572–578, [https://doi.org/10.1175/1520-0426\(1994\)011<0572:MOADRD>2.0.CO;2](https://doi.org/10.1175/1520-0426(1994)011<0572:MOADRD>2.0.CO;2).
- Li, X., J. A. Zhang, X. Yang, W. G. Pichel, M. DeMaria, D. Long, and Z. Li, 2013: Tropical cyclone morphology from spaceborne synthetic aperture radar. *Bull. Amer. Meteor. Soc.*, **94**, 215–230, <https://doi.org/10.1175/BAMS-D-11-00211.1>.
- Lorsolo, S., J. L. Schroeder, P. Dodge, and F. D. Marks, 2008: An observational study of hurricane boundary layer small-scale coherent structures. *Mon. Wea. Rev.*, **136**, 2871–2893, <https://doi.org/10.1175/2008MWR2273.1>.
- Montgomery, M. T., and R. J. Kallenbach, 1997: A theory for vortex Rossby waves and its application to spiral bands and intensity changes in hurricanes. *Quart. J. Roy. Meteor. Soc.*, **123**, 435–465, <https://doi.org/10.1002/qj.49712353810>.
- Morrison, I., S. Businger, F. Marks, P. Dodge, and J. A. Businger, 2005: An observational case for the prevalence of roll vortices in the hurricane boundary layer. *J. Atmos. Sci.*, **62**, 2662–2673, <https://doi.org/10.1175/JAS3508.1>.
- Nakanishi, M., and H. Niino, 2012: Large-eddy simulation of roll vortices in a hurricane boundary layer. *J. Atmos. Sci.*, **69**, 3558–3575, <https://doi.org/10.1175/JAS-D-11-0237.1>.
- Nolan, D. S., 2005: Instabilities in hurricane-like boundary layers. *Dyn. Atmos. Oceans*, **40**, 209–236, <https://doi.org/10.1016/j.dynatmoce.2005.03.002>.
- Reasor, P. D., M. D. Eastin, and J. F. Gamache, 2009: Rapidly intensifying Hurricane Guillermo (1997). Part I: Low-wavenumber structure and evolution. *Mon. Wea. Rev.*, **137**, 603–631, <https://doi.org/10.1175/2008MWR2487.1>.
- Rotunno, R., and G. H. Bryan, 2012: Effects of parameterized diffusion on simulated hurricanes. *J. Atmos. Sci.*, **69**, 2284–2299, <https://doi.org/10.1175/JAS-D-11-0204.1>.
- Sapp, J. W., S. J. Frasier, J. Dvorsky, P. S. Chang, and Z. Jelenak, 2013: Airborne dual-polarization observations of the sea surface NRCS at C-band in high winds. *IEEE Geosci. Remote Sens. Lett.*, **10**, 726–730, <https://doi.org/10.1109/LGRS.2012.2220118>.
- , S. O. Alsweiss, Z. Jelenak, P. S. Chang, S. J. Frasier, and J. Carswell, 2016: Airborne co-polarization and cross-polarization observations of the ocean-surface NRCS at C-band. *IEEE Trans. Geosci. Remote Sens.*, **54**, 5975–5992, <https://doi.org/10.1109/TGRS.2016.2578048>.
- Schubert, W. H., M. T. Montgomery, R. K. Taft, T. A. Guinn, S. R. Fulton, J. P. Kossin, and J. P. Edwards, 1999: Polygonal eyewalls, asymmetric eye contraction, and potential vorticity mixing in hurricanes. *J. Atmos. Sci.*, **56**, 1197–1223, [https://doi.org/10.1175/1520-0469\(1999\)056<1197:PEAECA>2.0.CO;2](https://doi.org/10.1175/1520-0469(1999)056<1197:PEAECA>2.0.CO;2).
- Smith, R. K., and M. T. Montgomery, 2010: Hurricane boundary-layer theory. *Quart. J. Roy. Meteor. Soc.*, **136**, 1665–1670, <https://doi.org/10.1002/qj.679>.
- Uhlhorn, E. W., and P. G. Black, 2003: Verification of remotely sensed sea surface winds in hurricanes. *J. Atmos. Oceanic Technol.*, **20**, 99–116, [https://doi.org/10.1175/1520-0426\(2003\)020<0099:VORSSS>2.0.CO;2](https://doi.org/10.1175/1520-0426(2003)020<0099:VORSSS>2.0.CO;2).
- , J. L. Franklin, M. Goodberlet, J. Carswell, and A. S. Goldstein, 2007: Hurricane surface wind measurement from an operational stepped frequency microwave radiometer. *Mon. Wea. Rev.*, **135**, 3070–3085, <https://doi.org/10.1175/MWR3454.1>.
- Ulbrich, C. W., and P. B. Chilson, 1994: Effects of variations in precipitation size distribution and fallspeed law parameters on relations between mean Doppler fallspeed and reflectivity factor. *J. Atmos. Oceanic Technol.*, **11**, 1656–1663, [https://doi.org/10.1175/1520-0426\(1994\)011<1656:EOVIPS>2.0.CO;2](https://doi.org/10.1175/1520-0426(1994)011<1656:EOVIPS>2.0.CO;2).
- Willoughby, H. E., and M. B. Chelmon, 1982: Objective determination of hurricane tracks from aircraft observations. *Mon. Wea. Rev.*, **110**, 1298–1305, [https://doi.org/10.1175/1520-0493\(1982\)110<1298:ODOHTF>2.0.CO;2](https://doi.org/10.1175/1520-0493(1982)110<1298:ODOHTF>2.0.CO;2).
- Wurman, J., and J. Winslow, 1998: Intense sub-kilometer boundary layer rolls in Hurricane Fran. *Science*, **280**, 555–557, <https://doi.org/10.1126/science.280.5363.555>.
- Zhang, J. A., K. B. Katsaros, P. G. Black, S. Lehner, J. R. French, and W. M. Drennan, 2008: Effects of roll vortices on turbulent fluxes in the hurricane boundary layer. *Bound.-Layer Meteor.*, **128**, 173–189, <https://doi.org/10.1007/s10546-008-9281-2>.
- , F. D. Marks, M. T. Montgomery, and S. Lorsolo, 2011a: An estimation of turbulent characteristics in the low-level region of intense Hurricanes Allen (1980) and Hugo (1989). *Mon. Wea. Rev.*, **139**, 1447–1462, <https://doi.org/10.1175/2010MWR3435.1>.
- , R. F. Rogers, D. S. Nolan, and F. D. Marks, 2011b: On the characteristic height scales of the hurricane boundary layer. *Mon. Wea. Rev.*, **139**, 2523–2535, <https://doi.org/10.1175/MWR-D-10-05017.1>.
- , D. S. Nolan, R. F. Rogers, and V. Tallapragada, 2015: Evaluating the impact of improvements in the boundary layer parameterization on hurricane intensity and structure forecasts in HWRF. *Mon. Wea. Rev.*, **143**, 3136–3155, <https://doi.org/10.1175/MWR-D-14-00339.1>.
- Zhu, P., 2008: Simulation and parameterization of the turbulent transport in the hurricane boundary layer by large eddies. *J. Geophys. Res.*, **113**, D17104, <https://doi.org/10.1029/2007JD009643>.
- , K. Menelaou, and Z.-D. Zhu, 2014: Impact of subgrid-scale vertical turbulent mixing on eyewall asymmetric structures and mesovortices of hurricanes. *Quart. J. Roy. Meteor. Soc.*, **140**, 416–438, <https://doi.org/10.1002/qj.2147>.